Ordered arrays of low-dimensional Au and Pd

synthesis and in situ observations

Abbondanza, Giuseppe

2022

Ordered arrays of low-dimensional Au and Pd

synthesis and in situ observations

Abbondanza, Giuseppe

2022

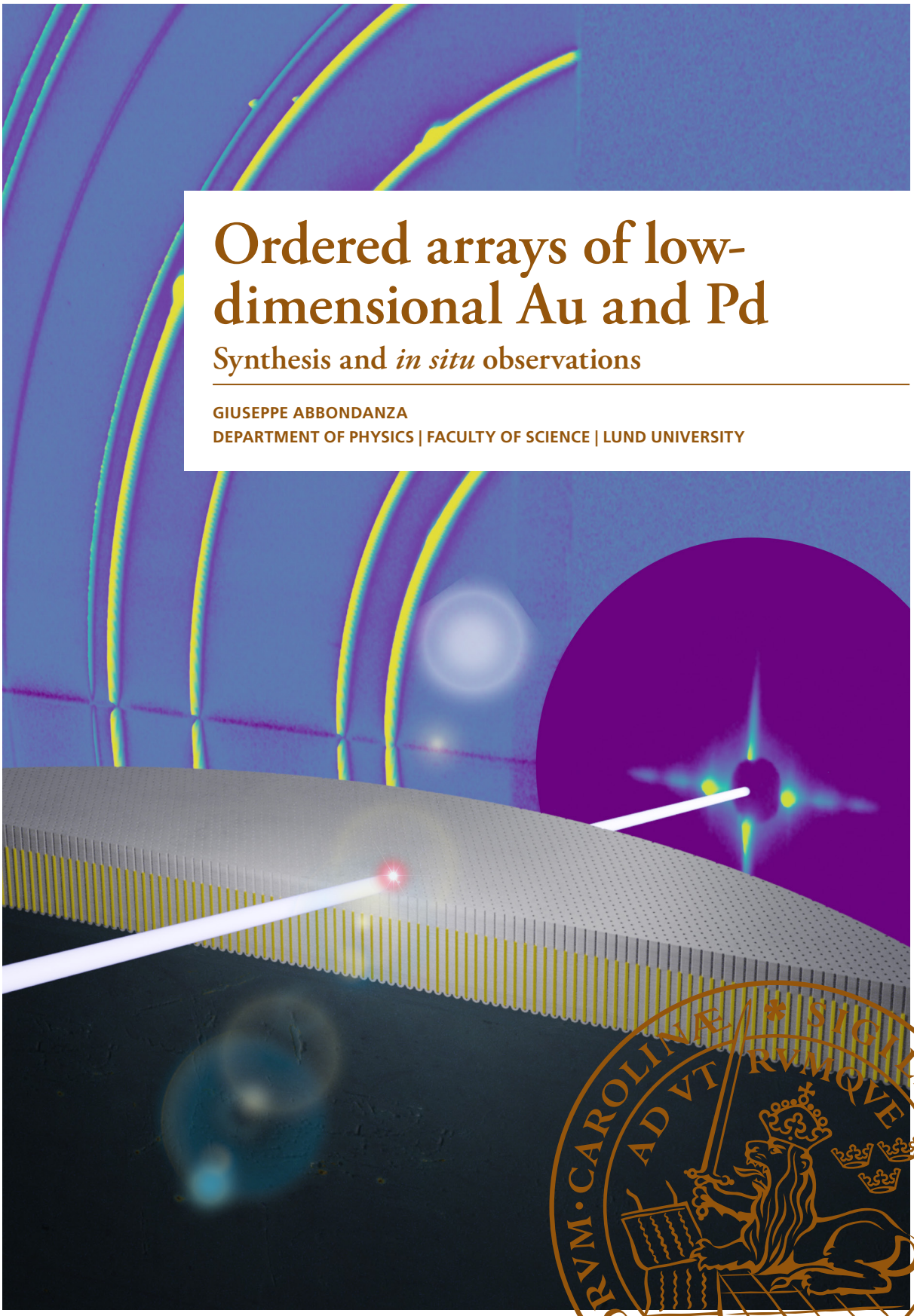

Ordered arrays of low-dimensional Au and Pd

Synthesis and *in situ* observations

GIUSEPPE ABBONDANZA
DEPARTMENT OF PHYSICS | FACULTY OF SCIENCE | LUND UNIVERSITY

Ordered arrays of low-dimensional Au and Pd

Synthesis and *in situ* observations

Ordered arrays of low-dimensional Au and Pd
Synthesis and *in situ* observations

by Giuseppe Abbondanza

LUND
UNIVERSITY

Thesis for the degree of Doctor of Philosophy
Thesis advisors: Prof. Edvin Lundgren, Dr. Gary S. Harlow, Prof. Magnus Borgström
Faculty opponent: Prof. Massimo Innocenti

To be presented, with the permission of the Faculty of Science of Lund University, in the Rydberg Lecture Hall on Friday, the 27th of January 2023 at 9:15.

Organization
LUND UNIVERSITY

Division of Synchrotron Radiation Research
Box 118
SE–221 00 LUND
Sweden

Document name
DOCTORAL DISSERTATION

Date of disputation
2023-01-27

Sponsoring organization

Author(s)
Giuseppe Abbondanza

Title and subtitle
Ordered arrays of low-dimensional Au and Pd: Synthesis and *in situ* observations

Abstract

Electrodeposition of metals in templates of nano-porous anodic aluminum oxide (NP-AAO) is a versatile way of fabricating ordered arrays of metal nanowires. Thanks to the self-arranged long-range hexagonal order of the pores, electrodeposition in NP-AAO is an easily scalable bottom-up synthesis route and an attractive alternative to traditional top-down fabrication methods such as electron beam lithography.

Since NP-AAO is a non-conductive medium and since it is potentially soluble in non-neutral pH solutions, the electrodeposition of metals in NP-AAO represents a challenge. These aspects are discussed in this thesis, aiming to establish a reproducible and reliable protocol for the electrodeposition of Au and Pd.

By using *ex situ* x-ray diffraction, it has been found that the growth of Au and Pd in the confined environment of nano-pores leads (i) to a deformation of the crystalline structure, as the lattice constant is smaller along the nanowire radius and larger along the nanowire axis, compared to the bulk lattice constant, and (ii) to a crystallite size anisotropy: it is limited by the pore radius in the horizontal direction and it is larger in the direction of growth.

The electrochemical growth of Au and Pd nanowires was followed *in situ* by x-ray scattering methods. In the case of Au nanowires, the time-resolved measurements revealed that the anisotropy of the lattice parameter progresses as a function of time, which suggests that the strain state of the nanomaterials can be artificially selected. This findings might be beneficial in the strain-engineering of Au nanoelectrode arrays for electrocatalysis. In the case of Pd nanowires, the measurements revealed strain variations, as well as phase transitions attributed to the existence of $\alpha-$ and $\beta-$phase Pd hydride in the NP-AAO template, due to the exposure of Pd to hydrogen evolved at the working electrode. These findings suggest that Pd in NP-AAO has potential applications in the design of hydrogen storage devices.

Key words
nanowires, nanorods, nanoparticles, Au, Pd, Al, Al_2O_3, anodization, nanoporous anodic aluminium oxide, powder x-ray diffraction, x-ray scattering, SAXS, WAXS, grazing incidence, 2-dimensional surface optical reflectance

Classification system and/or index terms (if any)

Supplementary bibliographical information

Language
English

ISSN and key title

ISBN
978-91-8039-480-2 (print)
978-91-8039-479-6 (pdf)

Recipient's notes

Number of pages
224

Price

Security classification

Signature _____ Date 2022-11-30

Ordered arrays of low-dimensional Au and Pd

Synthesis and *in situ* observations

by Giuseppe Abbondanza

LUND
UNIVERSITY

Cover illustration front: An x-ray beam illuminates an ordered array of Au nanowires in nano-porous anodic alumina using the grazing-incidence transmission geometry and generates scattering patterns.

Funding information: The thesis work was financially supported by the Swedish Research Council.

Faculty of Science, Division of Synchrotron Radiation Research

ISBN: 978-91-8039-480-2 (print)
ISBN: 978-91-8039-479-6 (pdf)

Printed in Sweden by Media-Tryck, Lund University, Lund 2023

Media-Tryck is a Nordic Swan Ecolabel certified provider of printed material. Read more about our environmental work at www.mediatryck.lu.se

MADE IN SWEDEN

Dedicated to
my wife Monica

Contents

List of publications and author contributions

This thesis is based on the following publications, referred to by their Roman numerals:

I **Quantitative powder diffraction using a (2+3) surface diffractometer and an area detector**
G. Abbondanza, A. Larsson, F. Carlá, E. Lundgren, G. S. Harlow
J. Appl. Cryst., 2021, **54**, pp. 1140–1152

I participated in developing the angle calculations and the correction factors, processed and analysed the data, prepared the figures and wrote the manuscript.

II **Electrochemical Fabrication and Characterization of Palladium Nanowires in Nanoporous Alumina Templates**
A. Larsson, G. Abbondanza, W. Linpé, F. Carlá, P. Mousley, C. Hetherington, E. Lundgren, G. S. Harlow
J. Electrochem. Soc., 2020, **167** (12), p. 122514

I contributed in planning and performing the XRD measurements, to the electrodeposition protocol and to the scientific discussion.

III ***In situ* scanning x-ray diffraction reveals strain variations in electrochemically grown nanowires**
A. Larsson, G. Abbondanza, L. Rämisch, W. Linpé, D. V. Novikov, E. Lundgren, G. S. Harlow
J. Phys. D: Appl. Phys., 2021, **54**, p. 235301

I participated to the XRD measurements and the scientific discussion.

IV **Templated electrodeposition as a scalable and surfactant-free approach to the synthesis of Au nanoparticles with tunable aspect ratios**
G. Abbondanza, A. Larsson, W. Linpé, C. Hetherington, F. Carlá, E. Lundgren and G. S. Harlow
Nanoscale Adv., 2022, **4**, pp. 2452-2467

I developed the fabrication route, operated the FIB-SEM, performed the XRD measurements, processed and analysed the data, prepared the figures and wrote the manuscript.

v ***In situ*** **hydride breathing during the electrochemical growth of Pd nanowires**
G. Abbondanza, A. Grespi, A. Larsson, D. Dzhigaev, L. Glatthaar, T. Weber, M. Blankenburg, Z. Hegedüs, U. Lienert, H. Over, G. S. Harlow, E. Lundgren
Manuscript submitted to *The International Journal of Hydrogen Energy*

I contributed in writing the beamtime proposal, planning and execution of the experiment. I processed and analysed the data, prepared the figures and wrote the manuscript.

vi **Anisotropic strain variations during the confined growth of Au nanowires**

G. Abbondanza, A. Grespi, A. Larsson, L. Glatthaar, T. Weber, M. Blankenburg, Z. Hegedüs, U. Lienert, H. Over, E. Lundgren
Short communication manuscript

I contributed in writing the beamtime proposal, planning and execution of the experiment. I processed and analysed the data, prepared the figures and wrote the manuscript.

vii **An electrochemical cell for 2-dimensional surface optical reflectance during anodization and cyclic voltammetry**
W. Linpé, G. S. Harlow, A. Larsson, G. Abbondanza, L. Rämisch, S. Pfaff, J. Zetterberg, J. Evertsson, and E. Lundgren
Rev. Sci. Instrum., 2020, **91**, p. 044101

I contributed to the design upgrade of the electrochemical cell, for use in combination with 2D-SOR.

Publications that are not included in the thesis, to which I have contributed during my PhD:

The State of Electrodeposited Sn Nanopillars within Porous Anodic Alumina from *in Situ* X-ray Observations
W Linpé, G. S. Harlow, J. Evertsson, U. Hejral, G. Abbondanza, F. Lenrick, S. Seifert, R. Felici, N. A. Vinogradov, and E. Lundgren
ACS Appl. Nano Mater., 2019, **2** (5), pp. 3031–3038

***Operando* Reflectance Microscopy on Polycrystalline Surfaces in Thermal Catalysis, Electrocatalysis, and Corrosion**
S. Pfaff, A. Larsson, D. Orlov, G. S. Harlow, G. Abbondanza, W. Linpé, L. Rämisch, S. M. Gericke, J. Zetterberg, E. Lundgren
ACS Appl. Mater. Interfaces, 2021, **13** (16), pp. 19530–19540

Revisiting Optical Reflectance from Au(111) Electrode Surfaces with Combined High-Energy Surface X-ray Diffraction
W. Linpé, L. Rämisch, G. Abbondanza, A. Larsson, S. Pfaff, L. Jacobse, J. Zetterberg, L. Merte, A. Stierle, Z. Hegedüs, U. Lienert, E. Lundgren, G. S. Harlow
J. Electrochem. Soc., 2021, **168** (9), p. 096511

Operando Stability Studies of Ultrathin Single-Crystalline IrO_2(110) Films under Acidic Oxygen Evolution Reaction Conditions
T. Weber, V. Vonk, D. Escalera-López, G. Abbondanza, A. Larsson, V. Koller, M. J. S. Abb, Z. Hegedüs, T. Bäcker, U. Lienert, G. S. Harlow, A. Stierle, S. Cherevko, E. Lundgren, H. Over
ACS Catal., 2021, **11** (20), pp. 12651–12660

Thickness and composition of native oxides and near-surface regions of Ni superalloys
A. Larsson, G. D'Acunto, M. Vorobyova, G. Abbondanza, U. Lienert, Z: Hegedüs, A. Preobrajenski, L. R. Merte, J. Eidhagen, A. Delblanc, J. Pan, E. Lundgren
Journal of Alloys and Compounds, 2022, **895**, p. 162657

HAT: A high-energy surface x-ray diffraction analysis toolkit

S. Pfaff, G. Abbondanza, Z. Hegedüs, U. Lienert, E. Lundgren, G. S. Harlow
Manuscript submitted to *J. Appl. Cryst.*

Popular science summary

Objects that have at least one dimension in the nanoscale are often referred to as "nano-" or "low-dimensional" materials in the scientific community. To give an idea of how small *nano* is, a nano-sized object next to a single hair would look like a blade of grass standing next to a skyscraper. In the last three decades, nanomaterials have been in the spotlight of fundamental and technological advances thanks to their extraordinary properties. Most of these properties stem from the fact that nanomaterials expose a considerable amount of surface to the surrounding environement: 1 g of spherical gold nanoparticles with a radius of 10 nm have a total surface area of about 16 m^2. Nanomaterials of precious metals like gold and palladium have been involved in the progress of numerous fields of science, such as electronics, optoelectronics, catalysis and biomedicine, to mention but a few.

Tremendous efforts from scientists all over the world have been made to learn how to fabricate gold and palladium nanomaterials, as well as to understand their formation, to learn and control their unique properties. In this thesis, a fabrication route is presented, which makes use of the so-called "template method". The template method consists in filling vertically aligned cylindrical nano-pores with metal, to obtain ordered arrays of nanoparticles or nanowires.

Little is known about the effect that the template method has on the properties of the nanomaterials. Based on our every-day experience, we could imagine that an object growing inside a nano-pore would deform and assimilate the shape of its container, just like the cubic tomato in Fig. 1, which grew inside in a box.

Figure 1: This tomato grew encased in a square box and deviated from its natural pathways of growth. Are nanowires grown in nano-porous templates subjected to a similar deformation? Part of this thesis aimed to answer this question. (Photo credits: moonimage/Flickr)

Some studies suggest that nanomaterials which were deformed just like the tomato above, have different properties than the ordinary undeformed ones. One way to quantify the extent of the deformation is to use x-ray diffraction. X-ray diffraction is a well-established technique that helps us to determine the distance between atoms. Nowadays, one can operate x-ray diffraction instruments routinely in a laboratory and learn about nanomaterials after they have been fabricated and often extracted from the environment where they formed. This approach is called an *ex situ* measurement.

Ideally, an x-ray diffraction measurement could run *while* the nanomaterials are forming atom by atom. However, the x-ray sources of conventional laboratories are too weak and the measurements are too slow, compared to the time-scale of the fabrication. Trying to capture the formation of nanomaterials with a common x-ray source would be like attempting to record a movie of a gymnast doing their routine by sketching frames by hand.

On the other hand, in synchrotron research facilities, very intense x-ray beams are generated. In fact, they are so intense that it becomes possible to perform experiments *in situ*, meaning that we can see the nanomaterials forming atom by atom in real time. In this thesis, synchrotron radiation was used to unravel the mysteries of the growth of nano-objects in confined environments.

Sommario divulgativo

Gli oggetti che hanno almeno una dimensione nella nanoscala vengono spesso chiamati dalla comunitá scientifica “nanomateriali” o materiali a “bassa dimensionalitá”. Per dare un’idea di quanto piccoli sono gli oggetti di cui stiamo parlando, un nanomateriale messo accanto a un capello avrebbe lo stesso aspetto di un filo d’erba accanto a un grattacielo. Negli ultim trent’anni, i nanomateriali sono stati al centro dello sviluppo scientifico fondamentale e tecnologico, grazie alle loro proprietá straordinarie. La maggior parte di queste proprietá deriva dal fatto che i nanomateriali hanno una quantitá notevole di superficie a contatto con l’ambiente circostante: 1 g di nanoparticelle sferiche di oro con diametro di 10 nm espone una superficie totale di 16 m^2. I nanomateriali di metalli preziosi come l’oro e il palladio sono coinvolti nel progresso di diversi campi scientifici come elettronica, optoelettronica, catalisi e biomedicina, per menzionarne solo alcuni.

Scienziati da tutto il mondo hanno ottenuto risultati eccezionali per sintetizzare nanomateriali di oro e palladio, ma anche per capire la loro formazione, per poter comprendere e controllare le loro uniche proprietá. In questa tesi é stato utilizzato il cosiddetto metodo “template”. Questo metodo consiste nel riempire nano-pori di forma cilindrica, allineati verticalmente, con metalli preziosi per ottenere matrici ordinate di nanoparticelle e “nanowires”.

L’effetto del metodo template sulle properietá dei materiali é quasi del tutto ignoto. In base alla nostra esperienza di tutti i giorni, potremmo immaginare che un oggetto che cresce in un nano-poro si deformi e assimili la forma del suo contenitore, proprio come il pomodoro in Fig. 2, che é cresciuto in una scatola cubica.

Alcuni studi suggeriscono che i nanomateriali che hanno subito deformazioni come il pomodoro hanno proprietá diverse rispetto a quelli non deformati. Un modo di quantificare questa deformazione é la diffrazione di raggi x. La diffrazione di raggi x é un metodo scientifico consolidato che ci aiuta a determinare la distanza tra gli atomi. Al giorno d’oggi, misurazioni di routine sono possibili in laboratori di fisica per studiare i nanomateriali dopo la loro sintesi e dopo che sono stati estratti dall’ambiente in cui si sono formati. Questo tipo di approccio é chiamato *ex situ*.

Figura 2: Questo pomodoro é cresciuto confinato in una scatola e la sua forma é diversa da quella di un normale pomodoro. I nanomateriali che crescono sotto nano-confinamento sono soggetti allo stesso tipo di deformazione? Lo scopo di parte di questa tesi é di rispondere a questa domanda. (Photo credits: moonimage/Flickr)

Idealmente, una misurazione di diffrazione di raggi x puó essere effettuata *mentre* i nanomateriali si stanno formando atomo per atomo. Tuttavia, le sorgenti di raggi x dei laboratori convenzionali sono troppo deboli e le misurazioni sono troppo lente rispetto ai comuni tempi di fabbricazione. Se provassimo a catturare la formazione dei nanomateriali con una sorgente di raggi x comune, sarebbe come provare a registrare il video di un esercizio di ginnastica olimpica disegnando i frame a mano libera.

Tuttavia, in un sincrotrone, vengono generati raggi x ad elevata intensitá. L'intensitá di questi raggi x é cosí alta che é possibile effettuare misurazioni *in situ*, il che significa che é possibile seguire la formazione dei nanomateriali atomo per atomo in tempo reale. In questa tesi, la radiazione di sincrotrone é stata usata per svelare i misteri della crescita di nanomateriali sotto confinamento.

Ordered arrays of low-dimensional Au and Pd: Synthesis and *in situ* observations

Chapter 1

Introduction

> "What would happen if we could arrange the atoms one by one the way we want them?"
>
> R. P. Feynman [1]

1.1 Motivation and background

Nanoscale materials of inorganic matter exhibit size-dependent physical-chemical properties that have enabled novel applications in computing, photonics, energy and biomedical technologies, in the last three decades [2–5]. The origin of the extraordinary qualities of nanomaterials lies in their size, composition and shape [6–9]. The idea that such aspects could be controlled in a systematic manner has driven the efforts of scientists and engineers from various communities such as physics, chemistry, materials science, surface science, etc.

The uniqueness of nanomaterials, compared to bulk materials, is due to the fact that they expose a higher fraction of atoms on the surface and that the charge carrier motion is confined to a smaller volume. Some of the size-dependent properties of nanomaterials include their lower melting point [10–12], possibility to trap crystalline

phases that are otherwise unstable in bulk [13] and widening of the band gap (in semiconductors) [14]. In noble metal nanomaterials whose size is smaller than the free electron mean free path, strong plasmon absorption bands arise from the collective oscillation of the electron gas on the nanomaterial surface [15–17]. In addition, noble metal nanocrystals exhibit unprecedented catalytic properties, due to the dominance of electronic surface states and the tunable size-dependent functionalities [18–22].

In this thesis, the focus is on Au- and Pd-based nanomaterials. Several research articles and reviews describe and characterize the most various bottom-up synthesis routes to fabricate nanoscale Au and Pd materials [19, 23, 24]. In most colloidal methods, the Au or Pd nanocrystals are synthesised in a liquid solution containing surfactants (or similar amphiphilic molecules) aggregates, whose role is to act as "nano-reactors" to guide the size and the morphology of the nanoscale metals and the same time to stabilize them in solution [25]. After the synthesis, the fabricated nanoparticles go through a stage of removal of the surfactants from their surfaces [26] (often referred to as "de-capping"), to enable applications where the availability of surface sites is relevant, e.g., in catalysis. In the scientific literature, this synthetic approach is called the *soft* template method [27].

An attractive alternative to the traditional colloidal synthesis is the *hard* template method [28–34]. The hard template method is a bottom-up technique where a membrane of vertically aligned nano-pores is filled with solid material, leading to the formation of nanoparticles, nanorods or nanowires with controlled size and morphology. This method is particularly advantageous since (i) it does not make use of surfactants, thus de-capping stages are not needed; (ii) it leads to ordered arrays of nanostructures, which is a sought-after feature in functional device applications [35]; (iii) the nanostructures can potentially be released in a solution, by selectively dissolving the template, exposing their extended surface area. Different methods aiming to fill the pores of a template have been proposed, which make use of gas- or liquid-phase solutions. The gas-phase fabrication routes are often based on chemical vapour deposition [36], while the liquid-phase ones often involve electroless- [37–39] or electro-deposition [28, 29].

However, studies that involve the template-assisted fabrication of nanostructures often

neglect the effect of growth in confined space. Although in literature some morphogenesis studies of materials under confinement can be found [40], only few of them are focused on nano-size-dependent effects [41, 42]. These studies support the hypothesis that the formation of material in nano-pores leads to a disturbance of the natural pathways of growth of a particular material and thus to mechanical deformations. The idea that we could control the mechanical deformation of nanomaterials by an appropriate template choice is particularly attractive in fields where the strain state is particularly relevant, such as in device design and catalysis [43, 44].

One way to investigate the strain state is by studying the atomic ordering and the pore filling using x-ray scattering methods. In principle such meausurements can be performed *ex situ* by using a laboratory source and a powder diffractometer. However, in order to study any anisotropy effect due to the confinement, a diffractometer with more rotational degrees of freedom, such as a surface diffractometer, is preferred. In principle, one could study the formation of nanostructures in a template in real-time while they are being synthesised. However, to measure a powder diffraction pattern using a laboratory source, with sufficient signal-to-noise ratio, measurement times in the order of at least 10-20 min are necessary. Such time scales are incompatible with the pace of the template-assisted growth. Thanks to the high brilliance of synchrotron radiation the time scale of the measurement is 1-5 s, which enables a whole class of *in situ* measurements.

1.2 This thesis

In this thesis, a method for the electrodeposition of Au and Pd in templates of nanoporous alumina is presented. The size, morphology and composition of the electrodeposited materials has been investigated by electron microscopies. Furthermore, x-ray scattering methods, both *in situ* and *ex situ*, have been used to explore the atomic ordering. Chapters 2 and 3 consist of an introduction to the materials and methods for the template preparation and the electrodeposition, explaining the underlying challenges and characteristics. Chapter 4 is a brief review of the characterization methods employed, while Chapter 5 consists of a summary of the results and an outlook into

future experiments. A collection of publications and manuscripts enclosed in the printed version of this thesis contains the main findings.

Chapter 2

Fundamentals of nano-porous anodic aluminum oxide templates

2.1 Introduction

When aluminum is exposed to ambient atmosphere, it is spontaneously coated by a thin layer of oxide (between 1.4 and 2.5 nm thick [45]). Further oxidation is prevented by the presence of this native oxide layer. However, when aluminum is "anodized", i.e., electrochemically oxidized in aqueous solution, a thicker layer than the native one can be formed, as it was first discovered by H. Buff (1857) [46]. Based on the nature of the electrolyte employed, a barrier-type or a porous-type oxide can be produced [47], as schematized in Fig. 2.1. Barrier-type AAO is usually formed in neutral electrolytes, while porous-type AAO is formed in acidic electrolytes [48]. In both cases a simple two-electrode setup like the one in Fig. 2.2 is used.

Masuda & Fukuda (1995) [49] found that under certain conditions of electrolyte composition, temperature and electric field, NP-AAO grows in a self-ordered hexagonal structure, with pores aligned with the surface normal of the aluminum substrate [49, 50]. It was later found by Nielsch et al. (2002) [29] that the self-ordered growth can only be sustained when the combination of pH, potential and electrolyte leads to a porosity of at least 10% and the volume expansion of alumina to aluminum is about

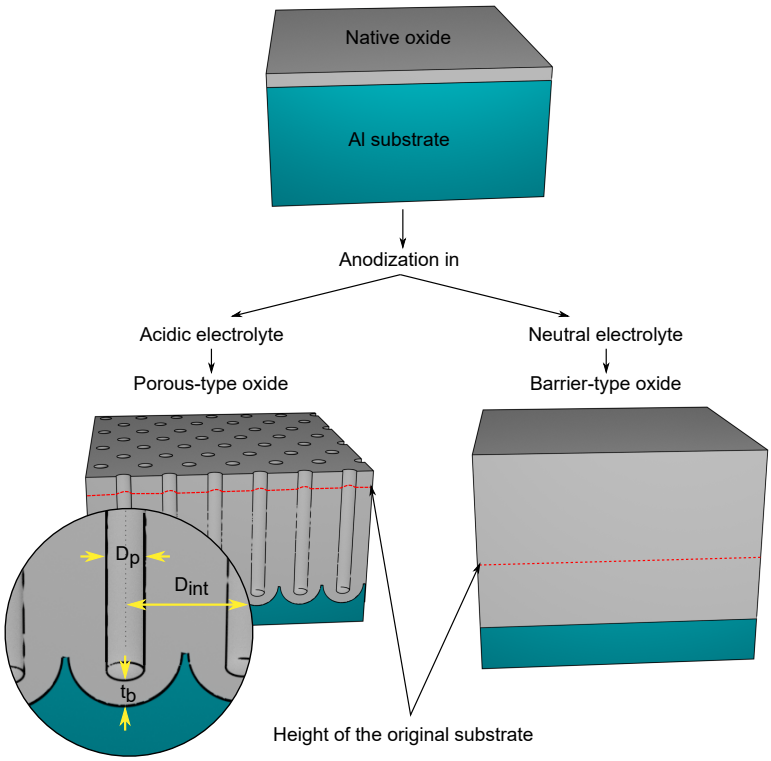

Figure 2.1: Based on the pH of the anodizing electrolyte, the alumina can grow as a porous- or barrier-type oxide. In the porous-type, the pore diameter (D_p), the inter-pore distance (D_{int}) and the thickness of the barrier layer (t_b) depend on conditions of anodizing voltage, electrolyte composition and concentration.

1.2. The inter-pore distance D_{int}, the pore diameter D_p and the thickness t_b of the oxide layer at the bottom of the pores, called the *barrier layer* (cfr. §3.1.1), are directly proportional to the electric potential U and are influenced by the choice of electrolyte [51]. Several experimentally derived equations relating U to D_{int}, D_p and t_b exist in literature for the most used anodizing electrolytes (sulphuric, oxalic and phosphoric acid) [52].

The NP-AAO template in an aqueous solution can be modelled as an electric circuit [53, 54] like the one in Fig. 2.3. Here, the barrier layer and the pore wall are each described by a resistor and a capacitor in parallel. The resistance of the electrolyte R_e in the pore is usually higher than that of the bulk solution R_{sol} as ion migration and mass transport in a nano-porous medium are subjected to a higher diffusional

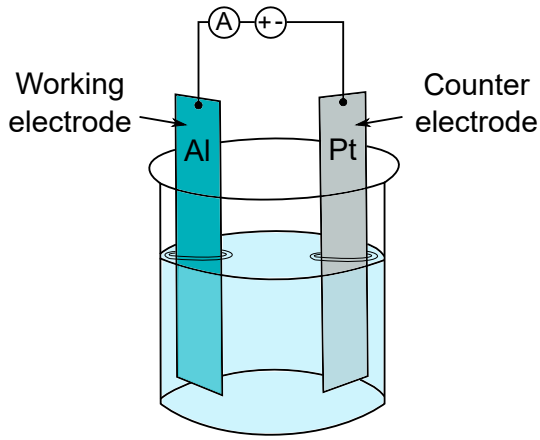

Figure 2.2: Illustration of an electrochemical two-electrode setup employed in the anodization of aluminum.

resistance [55].

The pores organize spontaneously in a hexagonal structure and the extent of the order depends on the anodization time. Longer anodization times lead to larger ordered porous domains and, as the newly formed oxide is produced at the bottom of the pores, the lower region is more ordered than the upper part. To fabricate a more uniformly ordered NP-AAO, the so-called two-step method can be used [50]. In this method, a first long (e.g., 10 h) anodization step yields a disordered hexagonal porous structure. Then, the oxide is selectively removed, usually by the action of a mixture of H_3PO_4 and H_2CrO_4, which results in an aluminum substrate patterned with hemisperical nano-concaves. Subsequently, a second anodization step is performed where the pore formation is guided by the presence of the nano-concaves and thus leads to a well-ordered NP-AAO template.

2.2 Electrochemical synthesis

NP-AAO templates are fabricated in the anodization of aluminum in a two-electrode electrochemical setup like the one illustrated in Fig. 2.2. The working electrode consists of a polished aluminum anode, while the counter-electrode is an inert electrode, e.g., a graphite rod or a Pt mesh. The electrolyte solution consists of a diluted acid,

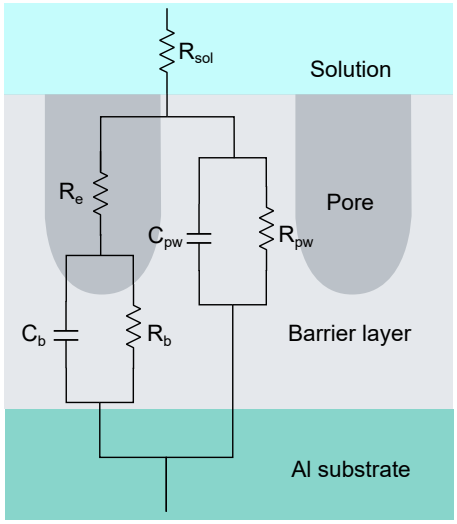

Figure 2.3: Equivalent circuit describing a template of nanoporous alumina exposed to an electrolyte solution. C_b and R_b are the capacitance and the resistance of the barrier layer, C_{pw} and R_{pw} are the capacitance and the resistance of the pore wall, R_{sol} and R_e are the resistance of the bulk solution and the electrolyte inside the pore, respectively. Diagram based on models found in refs. [53, 54].

e.g., sulfuric, phosphoric or oxalic acid [49, 50, 56].

The high electric field employed in the anodization drives the electrochemical reaction as well as the migration of Al^{3+} cations and O^{2-} or OH^- anions across the electrolyte/oxide/metal interface [57–59]. The key reactions that occur during the anodization are illustrated in Fig. 2.4. At the metal/oxide interface of the working electrode, the following reactions occurr [52]:

Oxidation of aluminum

$$Al_{(s)} \longrightarrow Al^{3+}_{(ox)} + 3\,e^- \tag{R1}$$

Formation of anodic oxide at the metal/oxide interface

$$2\,Al^{3+}_{(ox)} + 3\,O^{2-}_{(ox)} \longrightarrow Al_2O_{3(s)} \tag{R2}$$

While at the oxide/electrolyte interface the following reactions are possible:

Dissociation of water

$$H_2O_{(l)} \longleftrightarrow H_{(aq)}{}^{+} + OH^{-}_{(aq)} \tag{R3}$$

or

$$H_2O_{(l)} \longleftrightarrow 2\,H_{(aq)}{}^{+} + O^{2-}_{(ox)} \tag{R4}$$

Formation of anodic oxide at the oxide/electrolyte interface

$$2\,Al^{3+}_{(ox)} + 3\,O^{2-}_{(ox)} \longrightarrow Al_2O_{3(s)} \tag{R5}$$

or

$$4\,Al^{3+}_{(ox)} + 6\,OH^{-}_{(aq)} \longrightarrow 2\,Al_2O_{3(s)} + 6\,H_{(aq)}{}^{+} \tag{R6}$$

Heterolytic dissociation of water

$$2\,H_2O_{(l)} \longrightarrow O^{2-}_{(ox)} + OH^{-}_{(ox)} + 3\,H_{(aq)}{}^{+} \tag{R7}$$

Furthermore, the following "side" reactions, which will decrease the current efficiency of the anodic oxide growth, occur simultaneously with reactions R1-7, at the electrolyte/oxide interface:

Heat-induced and/or field-induced oxide dissolution

$$Al_2O_{3(s)} + 6\,H_{(aq)}{}^{+} \longrightarrow 2\,Al^{3+}_{(aq)} + 3\,H_2O_{(l)} \tag{R8}$$

Ion ejection from oxide to electrolyte

$$Al^{3+}_{(ox)} \longrightarrow Al^{3+}_{(aq)} \tag{R9}$$

Oxygen evolution

$$2\,O^{2-}_{(ox)} \longrightarrow O_{2(g)} + 4\,e^{-} \tag{R10}$$

The overall anodic reaction can be described as [60]:

$$2\,Al_{(s)} + 3\,H_2O_{(l)} \longrightarrow Al_2O_{3(s)} + 6\,H_{(aq)}{}^{+} + 6\,e^{-}. \tag{R11}$$

As the NP-AAO grows and the oxide growth front proceeds into the substrate, the aluminum anode is consumed. However, the aluminum oxide can be formed at the

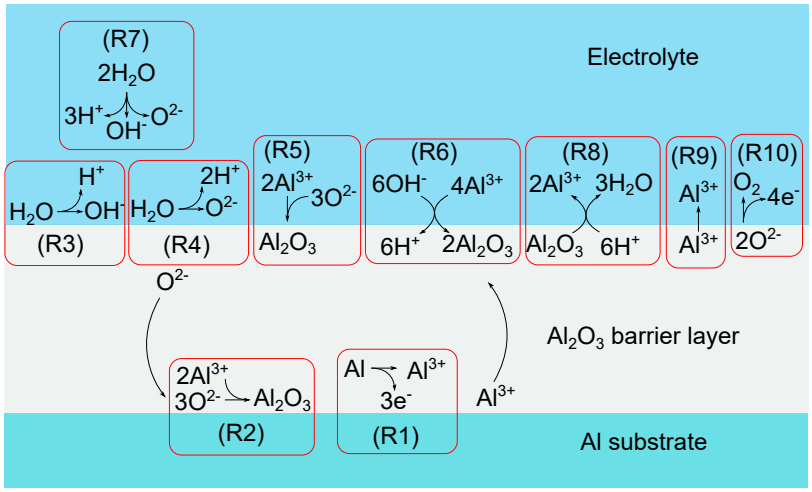

Figure 2.4: Summary of the key anodic reactions involved in the electrochemical synthesis of Al_2O_3. The reactions apply to both the growth of barrier- and porous-type oxide.

oxide/electrolyte interface, upon the migration of Al^{3+} under the action of the electric field. Since the anodic oxide is less dense than the aluminum, the total thickness of the NP-AAO and the underlying aluminum will be larger than the dimensions of the original substrate. Approximately, 60% of the total NP-AAO thickness will extend outside the original substrate surface.

At the very beginning of the anodization in acidic electrolyte, a compact barrier oxide film is formed. Tensile stress, imperfections and impurities are believed to cause cracks in the oxide and a local increase of the electric field. The electrolyte penetrates the cracks and the higher electric field polarizes the Al-O bonds, promoting the field-assisted dissolution of oxide [48, 51]. The cracks develop into small disordered pores, which grow in diameter or merge with neighbouring pores [61, 62]. Progressively, the pores rearrange to a steady-state self-ordered growth.

The origin of the steady-state pore formation is still an object of debate. Experimental evidences showed that the oxide growth proceeds at the metal/oxide interface only and that Al^{3+} ions migrating to the electrolyte/oxide interface are ejected to the solution without contributing to the oxide formation [63]. Two models have been proposed to explain this evidence. In the first model, the pore formation is driven by mechanical stress, due to electrostriction and volume expansion, which causes a vis-

cous flow of oxide from the pore bottom to the pore walls [64]. In the second model, the growth is driven by a field-assisted oxide decomposition at the oxide/electrolyte interface and oxide formation at the metal/oxide interface. The simultaneous progress of the metal/oxide and the oxide/electrolyte interfaces into the aluminum substrate determine the pore formation [61, 62]. The nature of the self-organization is not fully understood, although it has been proposed that if there is any oxide flow stress, repulsive forces between neighboring pores could mitigate the mechanical deformations. These repulsive forces are believed to drive the self-organization [29, 65].

2.3 Functionalization of NP-AAO

The possibility to grow nanomaterials using NP-AAO as a template is an outstanding application that has been increasingly attracting the interest of research groups in the last 20 years. The template-assisted synthesis of nanostructured functional materials is a relatively simple and cost-effective way of fabricating identical ordered nanostructures with well-defined size and shape. It is a bottom-up method that overcomes many drawbacks of state-of-the-art lithography and has potential applications in the assembly of hierachical architecture for device applications [52].

The synthesis of nanomaterials in hard nano-porous templates is robust and reproducible and it is particularly advantageous as the size and the shape of the synthesised nanostructures is dictated by the size and the shape of the pores [66]. Extensive research has been done on nano-porous systems as templates for the synthesis of metals, as well as polymers and semiconductors [52, 66, 67]. The fabrication can be approached with different techniques such as chemical vapor deposition, physical vapor deposition, sol-gel deposition, reactive ion etching and electrochemical/electroless deposition. In this thesis NP-AAO templates were used to fabricate Au and Pd nanostructures by means of electrochemical deposition.

Chapter 3

Electrodeposition into nano-porous anodic aluminum oxide templates

3.1 Electrodeposition in NP-AAO: challenges

3.1.1 Barrier layer

At the bottom of each pore there is a layer of Al_2O_3 referred to in literature as the "barrier layer". The thickness of the barrier layer depends on the electrolyte and the potential used in the anodization. Although this layer is electrically insulating, electrons can tunnel through it if it is sufficiently thin, or hop between impurity states and ionic defects in the oxide [68, 69]. Fig. 2.3 represents the circuit model of a NP-AAO template in an aqueous solution. Generally, the conductivity and the capacitance of an aluminum oxide film are inversely proportional to its thickness. Here, since the pore walls are several microns thick, it is often approximated by an infinite resistance R_{pw} and a zero capacitance C_{pw}. On the other hand, The resistance R_b and the capacitance C_b of the barrier layer cannot be neglected. To increase the chances of a successful electrodeposition, one could decrease the thickness of the barrier layer (as discussed later in §3.2) and use an AC potential to induce a displacement current through the capacitor C_b.

3.1.2 Solubility of NP-AAO

The Pourbaix diagram in Fig. 3.1 shows the possible stable phases predicted by thermodynamics as a function of pH and potential of the aqueous electrochemical system with an Al electrode [60, 70, 71]. From this diagram it appears that Al_2O_3 is insoluble in solutions with a pH in the 4-8 range: in acidic or alkaline environment the NP-AAO templates could dissolve. Therefore, one should keep in mind that the electrodeposition bath chosen should have a compatible pH to avoid damaging the template. If damage happens, the electrolyte will wet the Al underlying the NP-AAO. The Al substrate has a much lower resistance than the one of the barrier layer, thus most of the current will flow through the exposed Al substrate, obeying Kirchoff's current law. At this point the pores will stop being filled and the metal will uniquely be deposited in the damaged regions.

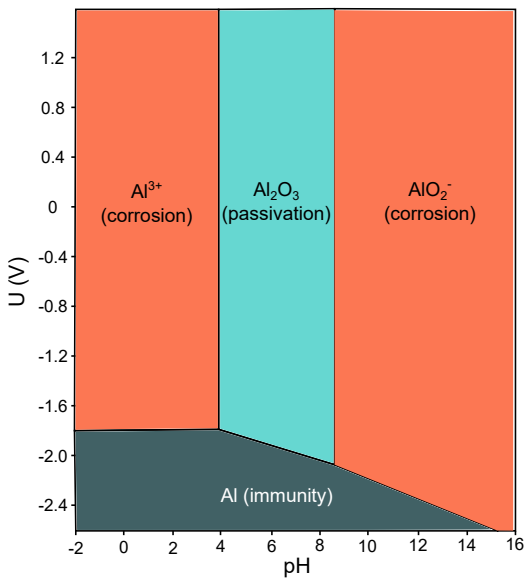

Figure 3.1: Pourbaix diagram of aluminum, correlating the conditions of pH and potential to the possible thermodynamically stable phases.

To avoid damaging the template one could (i) choose an electrodeposition bath with neutral pH and (ii) thermally anneal the template. Annealing the NP-AAO has proven to mitigate the deterioration by acids as strong as HF [72].The pH neutral-

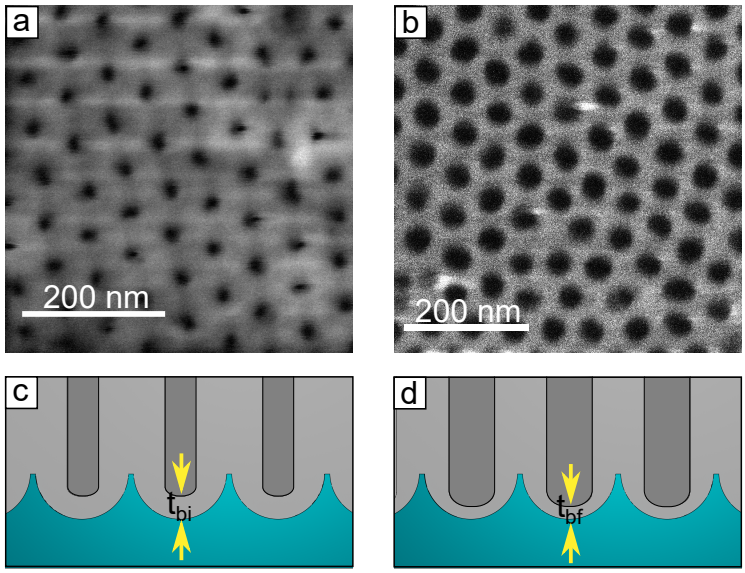

Figure 3.2: SEM micrographs of a template of porous alumina anodized in H_2SO_4 before (a) and after (b) pore widening in 5 w% H_3PO_4 at 30 ° C for 6 min. The isotropical wet-etching effect results in a thinning of the barrier layer from an initial value t_{bi} to a final value t_{bf}.

ity can be achieved by, e.g., a phosphate buffer solution. A buffer solution has the additional advantage to maintain pH neutrality during the electrodeposition pulses (see §3.3.2), where H^+ (OH^-) can be produced at the working electrode during the anodic (cathodic) pulses.

3.2 Template preparation strategies

The electrically insulating barrier layer at the bottom of the pores is one the main factors hindering the electrodeposition in NP-AAO. Several authors have proposed methods to thin or even remove the barrier layer and some of these methods are here reported.

3.2.1 Pore widening

The pore widening consists of a wet-chemical etch, usually by the action of an aqueous solution of H_3PO_4, where the pores are partially dissolved [73–75]. Since the etch is isotropical, the alumina dissolution leads to thinner pore walls and barrier layer. The etching rate is proportional to the temperature and the acid concentration; the total amount of alumina dissolved is time-dependent. Therefore, it is common to heat a solution, while stirring it, to a certain temperature and then immerse a sample of NP-AAO for a fixed amount of time. In this thesis, a solution of 5 w% H_3PO_4 heated at 30 $^\circ$ C was used. Fig. 3.2 shows the effect such pore widening protocol on a template fabricated in H_2SO_4, before (a) and after (b) pore widening for 6 min. The etching leads to an increase of pore diameter and to a decrease of the barrier layer thickness t_b from an estimated initial value of 25 nm to an estimated final value of 12 nm (the derivation of this value is shown in Paper IV), as illustrated in Fig. 3.2 (c) and (d). It has been proposed that pore widening causes the exposure of anions encapsulated in the inner walls of anodic alumina [76]. These anions have proved to enhance tunneling effects of conduction across the anodic oxide [77], thus facilitating the electrodeposition. One should bear in mind that an excessive etching duration can be detrimental to the integrity of the template. The pore widening method has been used in the synthesis of the Au nanostructures in Paper IV.

3.2.2 Electrochemical barrier layer thinning

It has been proved that the thickness of the barrier layer is proportional to the anodizing potential. For NP-AAO templates anodized in different electrolytes, it was found that $t_b/\Delta U \approx 1.2$ nm V^{-1} [78], where t_b is the thickness of the barrier layer and ΔU is the anodizing voltage. The electrochemical barrier layer thinning is based on this principle: at the end of the anodization, the applied potential is slowly reduced stepwise to an arbitrary value like in Fig. 3.3 [28, 79]. The final anodizing voltage will define the final thickness of the barrier layer. In contrast to pore widening, this leads to the formation of Y-shaped dendritic branches at the bottom of the pores. Consequently, any deposition of metal in the template will lead to branched nanowires. This preparation method has been used for the fabrication of Pd and Au nanowires

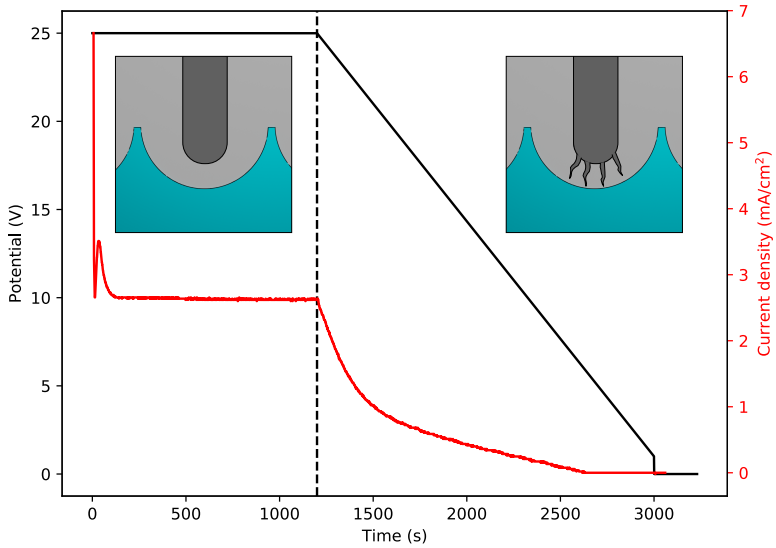

Figure 3.3: Applied potential (black) and measured current density (red) measured during a typical anodization and subsequent electrochemical barrier layer thinning. The dashed line denotes the start of the electrochemical barrier layer thinning.

in Papers II and IV, respectively.

3.2.3 Removal of the NP-AAO from the native Al substrate

Fig. 3.4 describes the steps involved in the barrier layer removal. The NP-AAO template can be removed from its native aluminum matrix by exposing the substrate to a selective etchant, e.g., a mixture of 0.1 M $CuCl_2$ in 20% HCl [80], or saturated $HgCl_2$ [81]. The back of the barrier layer can be directly exposed to 5% H_3PO_4 for sufficient time to form openings in the membrane (note that in contrast to the pore widening method in section §3.2.1, this does not necessarily lead to a larger pore diameter). In order to proceed to electrodeposition, a metal layer of Au, Ag or Pt needs to be sputtered or evaporated on one of the sides of the membrane, which will act as the working electrode [81, 82]. Although the absence of a barrier layer facilitates the electrodeposition, the increased number of steps in the production of the template and the handling of a thin and brittle alumina membrane (thickness ranging from 10 to 50 μm) potentially increases the difficulty of the fabrication. In addition, adhesion thin layers (e.g., a 5 nm Ti layer [83] or a 20 nm Cr layer [84]) are often required to

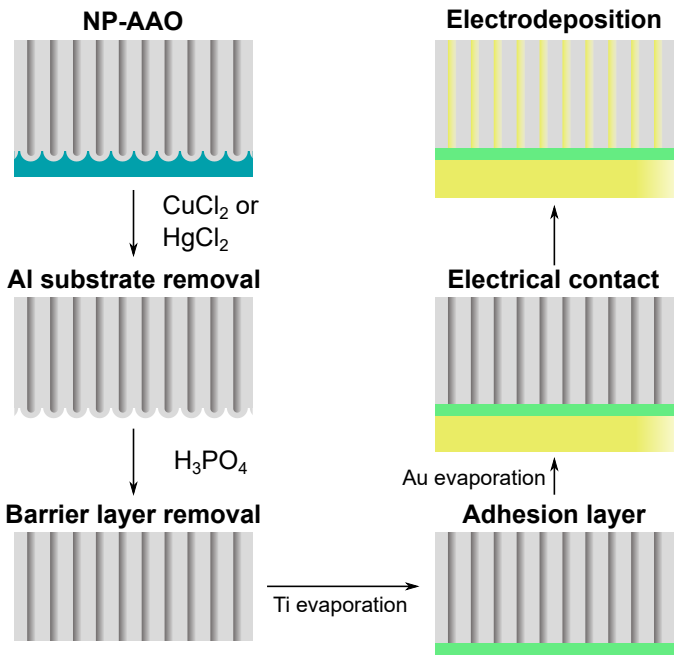

Figure 3.4: Stages in the removal of a NP-AAO membrane from its native Al substrate.

ensure the adherence of the electrode metal to the membrane. The addition of non-noble metals can potentially contaminate and alter the electrochemistry of the system during the electrodeposition and in possible applications.

3.3 Electrodeposition strategies

3.3.1 Limitations of DC and AC electrodeposition

DC electrodeposition in NP-AAO templates is most commonly viable when the barrier layer has been completely removed [81, 82, 84] (see §3.4), because of its high resistance (ranging from 10^{10} to 10^{15} Ω [53]). However, there are cases where the template has not been separated from the aluminum matrix and DC electrodeposition has proved to work, prior electrochemical barrier layer thinning by stepping the potential down to 1 V [85]. Nonetheless, the continuous application of electric poten-

tial causes template damage due to ohmic heating or aluminum oxide (or hydroxide) dissolution.

In contrast, the electrodeposition process and the template integrity benefit from AC methods. When an AC potential is applied, displacement currents are generated across the barrier layer, as the metal/oxide/electrolyte interface acts as a capacitor [53, 54]. Furthermore, since aluminum is a valve metal, its oxide has rectifying properties: it only allows conduction when a cathodic potential is applied [52, 86]. This implies that any metal cation in a pore can be reduced during the cathodic half-waves but the deposited metal cannot be oxidized during the anodic half-waves. Although AC methods are beneficial to the electrodeposition process, it leads to relatively small crystallite sizes of the deposited metal, damage of the template cause by ohmic heating (since high potentials are required, e.g., 20-35 $V_{peak-to-peak}$), poor and irregular pore-filling [87]. Therefore, more advanced methods like pulsed electrodeposition were developed.

3.3.2 Pulsed electrodeposition

Pulsed electrodeposition is a well-suited and efficient method to electrodeposit metals in NP-AAO templates. It consists in periodically applying a single AC potential wave, of typical frequency ranging from 100 Hz to 1 KHz, followed by a rest time, which ranges from 100 ms to 1 s [28, 88]. The potential and the current density deriving from a typical electrodeposition pulse are plotted in Fig. 3.5. During the cathodic half-wave the metal cations in the pores are reduced and the pore is thus depleted of reagent. During the anodic half-wave, the capacitance of the barrier layer is discharged. The rest time is introduced to allow replenishment of metal cations in the pores by means of diffusion. Paper II contains a simulation of how the concentration distribution along the pore length changes as a function of time, during the rest period. In contrast with DC and AC methods, pulsed electrodeposition is not mass-transfer limited, provided that the rest time is long enough. It has been found in the case of Cu electrodeposition in NP-AAO, that the deposited material has superior pore-filling when a square wave is used, instead of a sine wave, and that it is beneficial to start the pulse with a cathodic half-wave rather than an anodic half-wave [87].

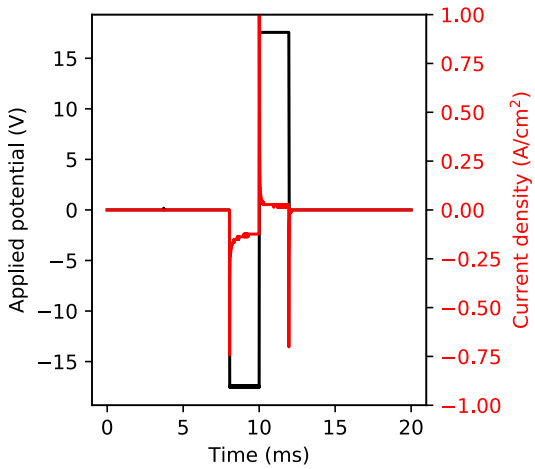

Figure 3.5: The cathodic (negative) half-waves of potential drive the electrodeposition of Au (black curve) and the resulting current density (red) is calculated from the voltage measured across a shunt resistor in series with the cell.

One should bear in mind that the electrodeposition is not the only reaction that is initiated by cathodic potentials. The hydrogen evolution reaction (HER, see §3.5) takes place at the working electrode when negative potentials are applied. In Paper V, the exposure of Pd nanowires in NP-AAO to hydrogen evolved during the electrodeposition led to the formation of Pd hydride phases.

3.4 Release of the nanostructures from the NP-AAO template

Noble metal nanoparticles or nanowires are of particular interest in fields such as heterogeneous catalysis because of their superior surface-to-volume ratio, as several interesting chemical transformations happen at the surface. Therefore, it might be desirable to release the encapsulated nanostructures in NP-AAO templates to enhance the accessibility to their surfaces and enable their applications. A solution of 1 M NaOH can be used to selectively dissolve the templates, as they are soluble outside the pH range of 4 to 8 (as discussed in §3.1.2).

In contrast to most colloidal synthetic routes for the fabrication of Au or Pd nanoparticles, the hard template method does not involve the use of surfactants. This is es-

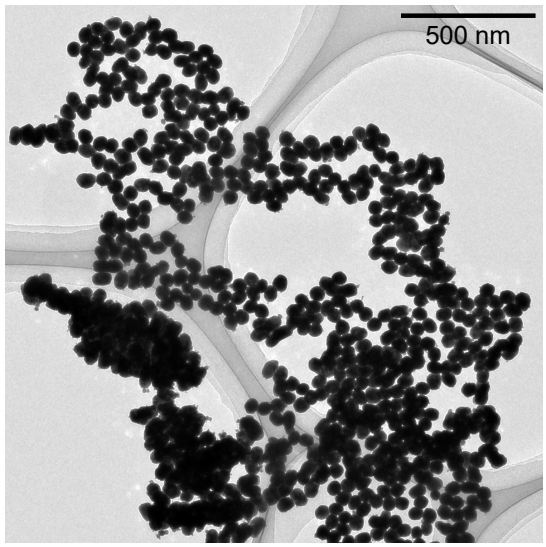

Figure 3.6: TEM image of Au nanoparticles released from the NP-AAO template.

pecially advantageous because it means that they do not need to undergo additional steps of de-capping, i.e., removal of surfactant to clear the surface, to enable, e.g., their catalytic properties.

3.4.1 Dispersed nanostructures in solution

Fig. 3.6 shows a TEM micrograph of Au nanoparticles released from a NP-AAO template. They were first released in a 1 M NaOH solution upon dissolution of the template, then 20 μL of solution were poured onto a TEM grid. With the hard template method, a precise control of size and aspect ratio is possible. However, to compete with the colloidal methods in terms of nanoparticle yield, working electrode areas of approximately 1-2 m^2 are necessary.

3.4.2 Up-standing arrays of nanostructures on a substrate

The hard template method has the exceptional advantage of yielding an ordered array of aligned up-standing nanostructures, such as those shown in Fig. 3.7. The steps of fabrication of these arrays are shown in Fig. 3.8. First, the pores were filled completely

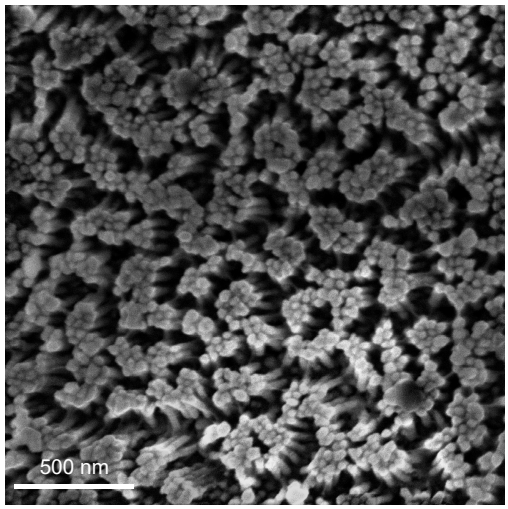

Figure 3.7: Top view of a forest of Au nanorods released from NP-AAO.

and the electrodeposition was continued to plate the template with a film of approximately 150-200 nm thick. The template was flipped upside down, positioned on a conductive substrate and selectively dissolved in 1 M NaOH. In our case, a piece of carbon tape was used as a conductive substrate for imaging purposes with electron microscopy. As an alternative to dissolving the template, one could grow Au nanowires until they emerge from the pore, like the ones in Fig. 3.9.

3.5 Electrochemical evolution of hydrogen

The electrodeposition of metals is not the only reaction that is driven by cathodic potentials in aqueous environments. For instance, the hydrogen evolution reaction (HER) [89], which is the half-reaction of water splitting, occurs simultaneously to electrodeposition when the cathodic half-waves of potential represented in Fig. 3.5 are applied to the working electrode, yielding H_2:

$$2H_{(aq)}{}^{+} + 2\,e^{-} \longrightarrow H_{2(g)}.$$

The use of renewable sources of energy to drive the HER potentially leads to a sustainable source of hydrogen fuel for zero-emission fuel cells [90, 91]. Furthermore, storing

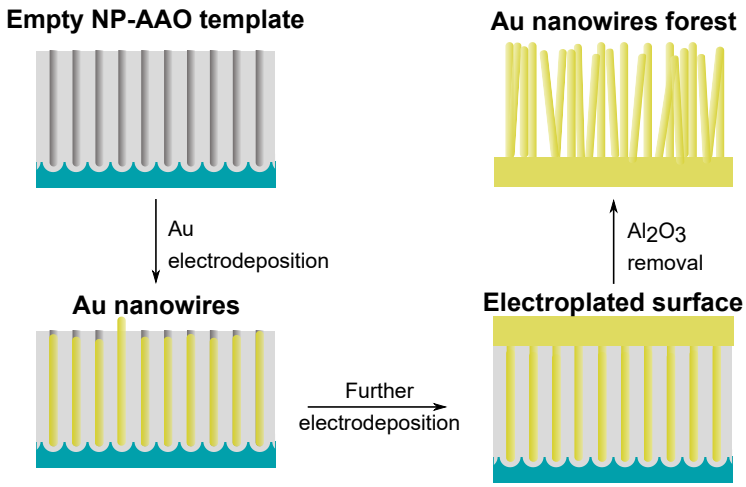

Figure 3.8: Steps involved in the fabrication of an up-standing array of Au nanowires.

electrochemically produced hydrogen in the solid form, in conditions of room temperature and ambient pressure [92, 93], is an innovative way of using the excess energy produced by intermittent green sources of energy such as solar and wind power. For this reason, extensive research is conducted on catalyst design aiming to minimize the overpotential needed to drive the HER and, often, nanomaterials are involved in the design of such catalysts [94, 95].

Pd-based materials and nanomaterials, for example, are known to have a high activity towards HER and to absorb large quantities of hydrogen in their crystal lattice [96]. The nano-size and the superior surface-to-volume ratio are also a way of contrasting the high costs of Pd: with an equal volume, Pd nanomaterials expose a larger number of surface active sites compared to bulk materials, leading to the enhancement of performances.

In Paper V, evidences of Pd hydrogenation during the electrochemical growth in NP-AAO have been found. They suggest that NP-AAO functionalized with Pd nanowires, is a promising framework for the design of devices dedicated to the electrochemical production and storage of hydrogen.

3.6 Size-dependent strain under confinement

In the scientific literature, a size-dependent lattice deformation in Sn nanowires electrodeposited in NP-AAO templates has been reported [97, 98]. The authors of this finding showed an expansion of the lattice constant in the direction of growth, which is inversely proportional to the pore radius. The tensile strain was attributed to a compression along the pore radius, due to the confinement, and a resulting elongation, due to the Poisson effect, along the nanowire axis. This studies suggested that the strain state of nanowires in NP-AAO can be tuned by selecting the pore radius, which is an attractive idea in many fields where the interatomic distances of the nanostructures are critical, e.g., in electrocatalysis [43, 99]. In fact, "strain-boosted" electrocatalysis has proven to enhance the activity, stability and selectivity of noble metals for the oxygen reduction reaction [100–102], hydrogen evolution reaction [103] and CO_2 reduction [104, 105].

However, very little is known about the stress building up during the templated electrodeposition, which causes such strain. In addition, the tensile strain reported in this study was extracted from conventional powder x-ray diffraction patterns (measured in the Bragg-Brentano geometry), where the scattering vector is normal to the sample surface. In order to access information on the direction of confinement and to verify the hypothesis that the strain along the pores radius is compressive, diffractometers with more rotational degrees of freedom are needed, such as the (2+3)-type surface diffractometer described in Paper I.

In the aforementioned work, the expansion was attributed to surface stress and growth stress. While the principles that govern surface stress are well-known, very little is understood about growth stress in confined environment. In the case of thin films on substrates, growth stress is caused by defects such as vacancies, interstitial atoms and dislocations, and it is constant under identical conditions of growth (pH, reduction potential and temperature) [106]. Therefore, it has been speculated that the size-dependent component of the surface stress is only due to anisotropic surface stress effects and that the growth stress is constant as a function of pore radius [98]. However, there are not enough experimental evidences to support this hypothesis and it is also unclear what the inter-play is between the stress and the cristallinity of the nanostruc-

tures [107]. Furthermore, it has never been considered that the growth stress could be due to deviations from the natural pathways of growth of a nanowire, as a response to the confinement along the radial direction. The stress and strain fields of a deformed object under constrains are well-described for macroscopic objects, but there is a lack of such studies at the nanoscale [108].

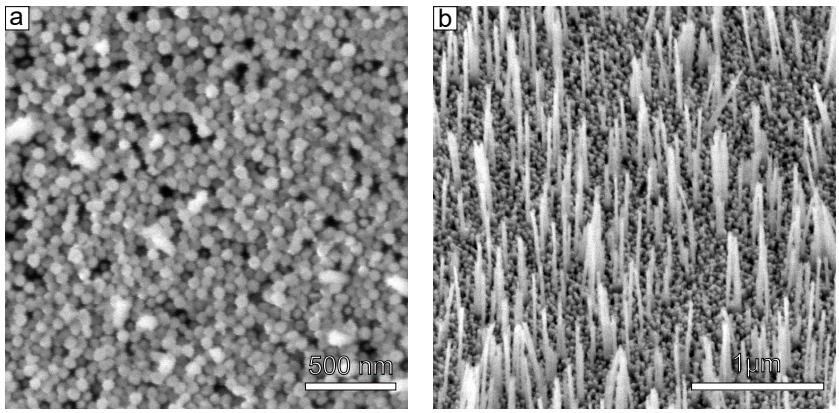

Figure 3.9: SEM micrographs: top view (a) and side view (b) of Au nanowires emerging from a NP-AAO template anodized in H_2SO_4.

Evidences of uniaxial size-dependent lattice expansion are in contrast with previous observation on unconstrained nanostructures, as anisotropic lattice contraction is the dominant effect amongst nanomaterials [109–112]. The anisotropic contraction is well explained by the bond-order-length-strength model as due to the coordination deficiency of the surface atoms, compared to the bulk atoms [113]. In fact, it has been shown in atomistic simulations that the surface atoms of a bulk-terminated Au nanowire reconstruct, causing a shrinking in diameter and length [114]. As many aspects about the growth in confined environment are unknown, *in situ* techniques are required to observe inter-atomic distances and the crystallinity of templated nanostructures during their formation.

Chapter 4

Experimental methods

4.1 X-ray diffraction

Due to the penetrative nature of x-rays into matter, x-ray based techniques are the most advantageous to study and characterize encapsulated nano-materials, such as the nanowires introduced in Chapter 3. This is especially true in the hard x-rays (20-40 keV) and high energy x-rays (60-100 keV) regimes, as photon attenuation by absorption decreases as a function of energy [115]. X-ray scattering methods at such high energies, are a class of photon-in-photon-out techniques that are particularly suitable for *in situ* studies under electrochemical conditions. For this reason x-ray diffraction has been the primary technique employed in this thesis, as it gives information on the structure and the inter-atomic distances of the studied material, in a non-destructive manner.

4.1.1 General concepts

The underlying physics that describes the nature of x-ray diffraction is well-known and its basic concepts have been first described more than a century ago. This section is a brief summary of these concepts and is based on textbooks describing the subject [116–118].

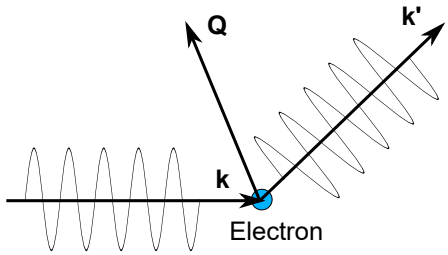

Figure 4.1: Vector representation of elastic scattering by an electron.

In the classic description, an electromagnetic wave with a wavelength in the x-ray regime strikes an electron, which is assumed to be free. The electron acts as an oscillator subjected to an external force and it is therefore subjected to an acceleration. Thus, it radiates a spherical wave of the same wavelength as the one of the incident wave. This is true only under the assumption of elastic scattering. The scattering differential cross-section of this photon-electron interaction is given by

$$\frac{d\sigma}{d\Omega} = r_0^2 |\hat{\epsilon} \cdot \hat{\epsilon'}|^2, \tag{4.1}$$

where $\hat{\epsilon}$ and $\hat{\epsilon'}$ are the polarization vectors of the incident and scattered wave, and r_0 is the classical electron radius, also known as the Thomson scattering length:

$$r_0 = \left(\frac{e^2}{4\pi\epsilon_0 mc^2} \right) = 2.82 \times 10^{-15} m. \tag{4.2}$$

Similarly, an atom can be illuminated by an x-ray. In this case, the scattering amplitude is calculated by summing up the contributions arising from the single electrons in the atom. In an atom with electron density $\rho(\mathbf{r})$, the contribution arising from the volume element $d\mathbf{r}$ is therefore $-r_0\rho(\mathbf{r})d\mathbf{r}$ and the scattering length of the whole atom can be expressed as

$$-r_0 f^0(\mathbf{Q}) = -r_0 \int \rho(\mathbf{r}) e^{i\mathbf{Q}\cdot\mathbf{r}} d\mathbf{r}, \tag{4.3}$$

where $e^{i\mathbf{Q}\cdot\mathbf{r}}$ is the phase factor attributed to the scattering vector $\mathbf{Q} = \mathbf{k}'\text{-}\mathbf{k}$, represented in Fig. 4.1, which relates the incident wavevector ($\mathbf{k}$) the the scattered one ($\mathbf{k}'$). Since we are only considering elastic scattering, $|\mathbf{k}| = |\mathbf{k}'|$.

When the energy of the incident x-rays is near the energy of an atomic absorption edge, the scattered amplitude deviates from that described in equation 4.3. The energy-dependence of the scattering amplitude is described by the dispersion correction factors $f'(\hbar\omega)$ and $f''(\hbar\omega)$:

$$f(\mathbf{Q}, \hbar\omega) = f^0(\mathbf{Q}) + f'(\hbar\omega) + if''(\hbar\omega). \tag{4.4}$$

While the real part of $f(\mathbf{Q}, \hbar\omega)$ describes the scattering length, the imaginary part is an expression of the x-ray attenuation by absorption.

In a crystalline material, atoms are arranged in a periodic structure which consists of a unit cell repeating itself in space. If we denote the position of the j-th atom inside a unit cell with the vector $\mathbf{r}_j$ and the position of the n-th unit cell with the vector $\mathbf{R}_n$, the position of any atom in the crystal lattice is denoted by the sum $\mathbf{R}_n + \mathbf{r}_j$. The scattering amplitude is hence described by the structure factor $F(\mathbf{Q}, \hbar\omega)$, expressed as

$$F(\mathbf{Q}, \hbar\omega) = -r_0 \sum_j f_j(\mathbf{Q}, \hbar\omega) e^{i\mathbf{Q}\cdot\mathbf{r}_j} \sum_n e^{i\mathbf{Q}\cdot\mathbf{R}_n}. \tag{4.5}$$

The structure factor $F(\mathbf{Q}, \hbar\omega)$ depends on the symmetry of the crystal, on the unit cell basis vectors ($\mathbf{a}_1$, $\mathbf{a}_2$, $\mathbf{a}_3$) and on a set of integers (n_x, n_y, n_z) through the following equation:

$$\mathbf{R}_n = n_x\mathbf{a}_1 + n_y\mathbf{a}_2 + n_z\mathbf{a}_3. \tag{4.6}$$

The second term in equation 4.5 is non-vanishing only when

$$\mathbf{Q} \cdot \mathbf{R}_n = 2\pi \times integer. \tag{4.7}$$

To find a solution, we describe any lattice site by a reciprocal lattice vector

$$\mathbf{G} = h\mathbf{a}_1^* + k\mathbf{a}_2^* + l\mathbf{a}_3^*, \tag{4.8}$$

where (h,k,l) are integers (called the Miller indices), and ($\mathbf{a}_1^*$, $\mathbf{a}_2^*$, $\mathbf{a}_3^*$) is the reciprocal lattice unit cell basis, related to the direct space unit cell basis through the relation $\mathbf{a}_i \cdot \mathbf{a}_j^* = 2\pi\delta_{ij}$, where δ_{ij} is the Kronecker delta. The scalar product between $\mathbf{G}$ and $\mathbf{R}_n$ yields

$$\mathbf{G} \cdot \mathbf{R}_n = 2\pi(hn_x + kn_y + ln_z) = 2\pi \times integer. \tag{4.9}$$

which means that the solution to equation 4.7 is the following expression, known as the *Laue condition*, i.e., the only condition at which diffraction occurs:

$$\mathbf{Q} = \mathbf{G}. \tag{4.10}$$

The structure factor in equation 4.5, may be expressed as

$$F(\mathbf{Q}) = \int_V \rho(\mathbf{r}) e^{i\mathbf{Q}\mathbf{r}} d\mathbf{r}, \tag{4.11}$$

where $\rho(\mathbf{r})$ is the electron density and the integral is extended over the whole volume V of the crystal. It should be noted that the structure factor in equation 4.11 can be seen as the Fourier Transform of the electron density. The Fourier Transform is a useful mathematical construct to relate the periodicity of a crystal lattice to the spatial frequency, which belongs to the domain of reciprocal space.

Another way of expressing the diffraction condition is given by Bragg's law, which describes the constructive interference between two scattered waves:

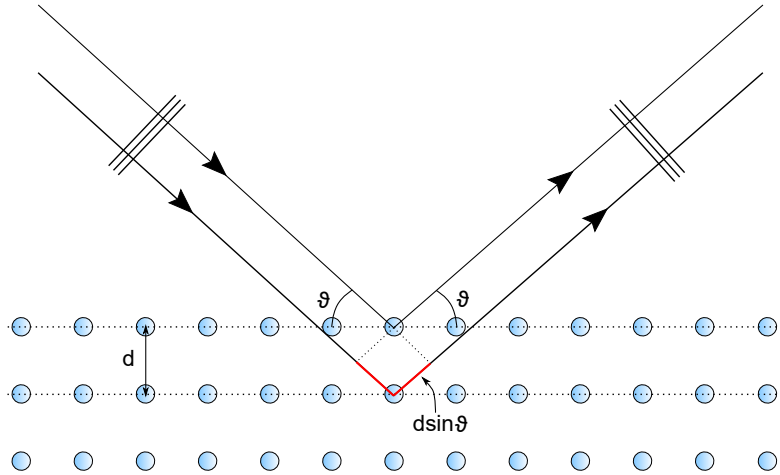

Figure 4.2: The Bragg formulation of diffraction describes the condition at which two scattered waves constructively interfere, in a mirror-like fashion.

$$m\lambda = 2d\sin\theta \tag{4.12}$$

where m is an integer, d is the separation between the atomic planes of interest and θ is the diffraction angle. A particular grain is said to be in the "Bragg condition" when the path difference of two adjacent scattered waves is a multiple integer of the x-ray wavelength. As the codomain of $\sin(\theta)$ is the interval [-1,1], $d \geq \frac{m\lambda}{2}$, which means that the smallest observable inter-atomic distance is limited by the wavelength of the radiation used, divided by two. As x-rays have usually a wavelength comparable with most inter-atomic distances, they are the kind of electromagnetic radiation compatible with diffraction experiments. Although Bragg's law does not provide information on the intensity of the diffracted x-rays, the square modulus of the structure factor is proportional to the diffracted x-ray intensity at any $\mathbf{Q}$ allowed by the symmetry of the system:

$$I(\mathbf{Q}) \propto |F(\mathbf{Q})|^2. \tag{4.13}$$

4.1.2 Powder x-ray diffraction

The construct based on infinite crystals discussed in the previous section does not match the reality of every crystalline system. Often, the order of the crystal lattice is broken by grain boundaries, amongst other kinds of defects. In a powder sample, several grains with random orientation are illuminated by an x-ray beam. Statistically, a certain number of these grains will happen to be in the Bragg condition (see §4.1.1). This will not give rise to a diffraction pattern with discrete Bragg reflections, but it will generate a diffraction *ring*, as represented schematically in Fig. 4.3. In this scenario, the scattered wavevector **k'** lies on the surface of a cone (known as the Debye-Scherrer cone) [119, 120].

If the orientation of the grains is purely random and isotropic, the intensity distribution along the ring will be homogeneous, while in textured materials the intensity is heterogeneously distributed. Therefore, the intensity along a diffraction ring is an expression of the preferential orientations of the grains.

A more descriptive intensity proportionality, compared to the one shown in equation 4.13, is

$$I(\mathbf{Q}) \propto M_{hkl}|F(\mathbf{Q})|^2 PL(\mathbf{Q})VT_{hkl}, \tag{4.14}$$

where M_{hkl} is an integer that depends on the symmetry of the crystal and on the (hkl) reflection, P is the polarization factor, L($\mathbf{Q}$) is the Lorentz factor, V is the interaction volume (which depends on the experimental geometry) and T_{hkl} is a factor that describes any preferential orientations. In a perfectly isotropic powder, $T_{hkl} = 1$ for every (h,k,l).

Powder x-ray diffraction is often performed in transmission geometry, using samples of flat plates and capillaries. Traditionally, point detectors are employed, which scan around the diffractometer centre using the Bragg-Brentano [121] or Debye-Scherrer [122] geometry. In the first case, both the sample incidence of the x-rays on a flat-plate sample and the detector angle are simultaneously scanned, in a so-called $\theta - 2\theta$ scan. In the second case, the detector is scanned while rotating around the capillary

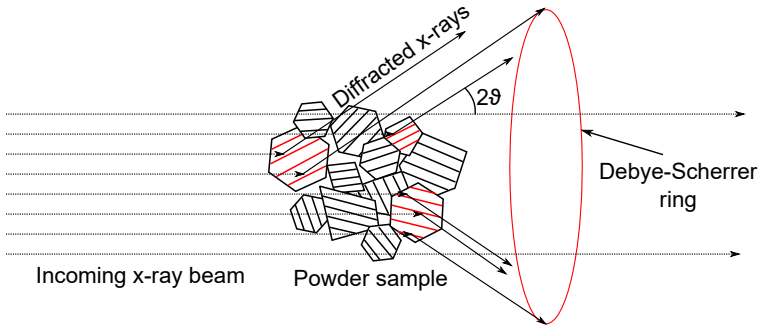

Figure 4.3: Some of the randomly oriented grains in a powder specimen fulfill the Bragg condition and give rise to diffraction rings.

axis. In this thesis, most of the work was done in the grazing-incidence geometry, where the incidence angle is fixed and an area detector is either scanned around the diffractometer centre or stands statically, facing the centre of the diffractometer.

4.1.3 Grazing-incidence geometry

The grazing-incidence geometry is an experimental configuration where the x-ray beam illuminates a specimen at small incidence angles, in order to control the penetration depth [118]. It is often used in surface x-ray diffraction to enable surface-sensitive experiments. In this thesis, however, the interest is oriented towards nanostructures encapsulated in nano-porous alumina and therefore, the grazing-incidence geometry is used as a tool to select an appropriate penetration depth to illuminate the nanostrucutres. The refractive index of the material is the link between the grazing-incidence angle and the x-ray penetration depth.

In the x-ray regime, the refractive index can be expressed as

$$n = 1 - \delta + i\beta, \tag{4.15}$$

where δ is an expression of the scattering length and β is an expression of the attenuation length. The refractive index is related to the dispersion-corrected scattering amplitude (equation 4.4) through the following:

$$n = 1 - \frac{2\pi\rho_{at}r_0}{k^2}[f^0(0) + f' + if''], \tag{4.16}$$

where ρ_{at} is the atomic density of the material (number of atoms per unit volume) and k is the wavenumber.

By comparing equations 4.15 and 4.16, we find the following relations for δ and β:

$$\delta = \frac{2\pi\rho_{at}r_0[f^0(0) + f']}{k^2} \tag{4.17}$$

$$\beta = -\frac{2\pi\rho_{at}r_0 f''}{k^2} \tag{4.18}$$

In addition, β is related to the attenuation coefficient μ through the following:

$$\beta = \frac{\mu}{2k}. \tag{4.19}$$

Usually, δ and β are in the order of 10^{-5} and 10^{-6}, respectively. This means that n < 1 and that total external reflection is possible when, e.g., x-rays travel from vacuum, or air, towards any investigated material.

Snell's law of refraction can be used to calculate the critical angle α_c, i.e., the angle that yields total external reflection, which is related to the material constant δ:

$$\alpha_c \approxeq \sqrt{2\delta}. \tag{4.20}$$

In the total external reflection condition, the incident wave exists in the form of an evanescent wave inside the material. The amplitude of such evanescent wave is dampened exponentially and the $1/e$ penetration depth Λ depends on the incidence angle α_i as follows [123]:

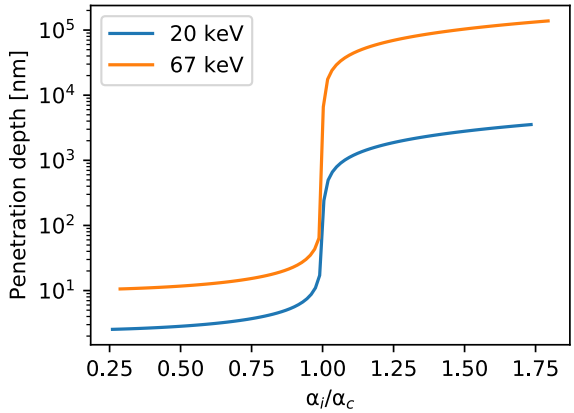

Figure 4.4: Penetration depth Λ of hard x-rays with an energy of 20 keV and high-energy x-rays with an energy of 67 keV into a semi-infinite slab of Al_2O_3, as a function of incidence angle α_i divided by the critical angle of total external reflection α_c.

$$\Lambda^{-1} = \frac{k}{\sqrt{2}}\{(2\delta - \sin^2\alpha_i) - [(\sin^2\alpha_i - 2\delta)^2 + 4\beta^2]^{1/2}\}^{1/2}. \tag{4.21}$$

The penetration depth Λ expressed in equation 4.21 is plotted in Fig. 4.4 as a function of the incidence angle α_i divided by the he critical angle of total external reflection α_c, calculated for beam energies of 20 keV and 67 keV, using tabulated values for δ and β. The overall penetration depth at high-energies (67 keV) is higher than in the hard x-rays regime (20 keV), due to the lower rate of interaction with matter.

The grazing-incidence geometry is particularly advantageous for the study of interfaces compared to, e.g., electron microscopy, due to the fact that (i) it averages information on sample size and morphology over a large area (the area illuminated by the x-ray beam), whereas microscopy only provides information on a selected small area, (ii) it does not require any particular sample preparation to study buried or encapsulated interfaces, while in electron microscopy a cross sectional area needs to be milled or a lamella needs to be extracted, and (iii) it allows *in situ* investigations under electrochemical conditions (and other sample environments).

4.1.4 Strain

The mechanical deformation of crystalline materials can be extracted from a diffraction pattern. The cause of such deformations can be an applied external load, residual stress or growth stress. The latter is the case in nanowires grown in confined environment.

Compressive or tensile deformation along a particular crystallographic direction results in an uniform variation of the lattice constant. This is the case of *homogeneous* strain. If the distance d between atomic planes vary, so will the diffraction angle predicted by Bragg's law (equation 4.12), leading to a shift of the peak positions from the theoretical bulk value of the unstrained material d_0, schematically represented in Fig. 4.5 (a) and (b). The strain can be then calculated as

$$\epsilon = \frac{d - d_0}{d_0}. \tag{4.22}$$

On the other hand, if the deformation leads to an uneven distribution of lattice constants, caused by an interstitial defect, vacancy or dislocation, as shown in Fig. 4.5 (c), a distribution of diffraction angles will fulfill Bragg's law and the width of the diffraction peaks will be affected. In this case, the strain is said to be *heterogeneous* [119]. In the assumption that the diffraction peak is described by a Voigt profile, the root-mean-square heterogeneous strain ϵ_{RMS} will contribute to the Gaussian component of the width by an amount Γ_s, expressed by equation 4.23:

$$\Gamma_s = 4\epsilon_{RMS} \tan\theta. \tag{4.23}$$

One should notice that, while the homogeneous strain can be positive or negative (depending if the strain is expansive or compressive), the heterogeneous strain is a measure of the overall deformation of the material, regardless of the strain direction.

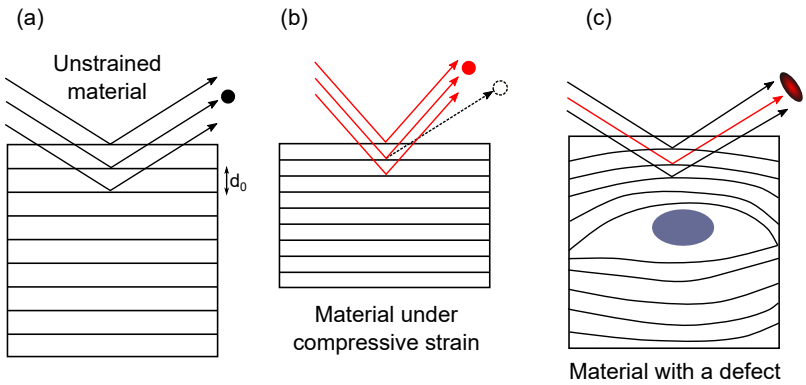

Figure 4.5: Schematic of the unstrained material (a), material undergoing homogeneous compressive strain (b), material with a defect that causes heterogeneous strain.

4.1.5 Crystallite size

Different crystallographic orientations meet at grain boundaries, as discussed in §4.1.2. The size of a grain, or crystallite, τ affects the Lorentzian component of the peak width as described by Scherrer equation [124]:

$$\tau = \frac{k\lambda}{\Delta 2\theta \cos\theta}, \tag{4.24}$$

where k is a dimensionless constant dependent on the shape of the crystallites (usually close to unity), λ is the wavelength of the incident x-rays, $\Delta 2\theta$ is the width of the diffraction peak expressed in radians, and θ is the peak position. In diffraction patterns reported as a function of the scattering vector Q, τ can be expressed as a function of the width of a peak ΔQ as

$$\tau = \frac{k2\pi}{\Delta Q}. \tag{4.25}$$

A common source of error in the estimation of the crystallite size is the spectral width of the source. Bragg's law (equation 4.12) works in the assumption that the incident x-rays are perfectly monochromatic. In reality, even monochromatic x-ray beams have a finite spectral widths $\Delta\lambda$. Differentiating Bragg's law with respect to λ, it can be

found that the spectral width has an impact on the spectral peak width $\Delta\theta_s$:

$$\Delta\theta_s = \frac{\Delta\lambda}{\lambda}\tan\theta. \tag{4.26}$$

The Lorentzian component Γ_L of the diffraction peak width is a sum of the contribution from the crystallite size and the spectral width:

$$\Gamma_L = \frac{k\lambda}{\tau\cos\theta} + \frac{\Delta\lambda}{\lambda}\tan\theta. \tag{4.27}$$

If we multiply every term in equation 4.27 by $\cos\theta$, we obtain

$$\Gamma_L\cos\theta = \frac{k\lambda}{\tau} + \frac{\Delta\lambda}{\lambda}\sin\theta. \tag{4.28}$$

A plot of $\Gamma_L\cos\theta$ as a function of $\sin\theta$ is called a Williamson-Hall plot [125]. With a linear fit of the Williamson-Hall plot, it is possible to separate the width contribution of the crystallite size (inversely proportional to the intercept) from the spectral width (proportional to the slope). An example of such analysis can be found in Papers I and IV.

4.1.6 Rietveld refinement: basic concepts

In the previous sections, we have seen that a lot of structural information is encoded in powder x-ray diffraction patterns. One way to access this information is Rietveld refinement. It consists in fitting the diffraction pattern with a theoretical model based on parameters such as: symmetry group of the phases present in a specimen, lattice constants, strain (both homogeneous and heterogeneous), size of the crystallites and preferential orientations. The area of the fitted peaks is not arbitrary but it has mathematical constraints based on the square modulus of the structure factor, fulfilling the proportionality in equation 4.14 [126–129]. The background can be part of the refinement, too, by including the coefficients of a Chebyshev polynomial as fitting parameters. A multitude of other parameters affecting the diffraction pattern can be

part of the refinement, such as the crystallographic occupancy, which describes the probability that a particular lattice site is occupied or not by an atom.

Rietveld refinement is based on a non-linear least square iterative algorithm that aims to minimize the difference between the observed intensity y_i^{obs} and the calculated model y_i^{calc} of the i-th data point as in the following equation:

$$M = \sum_i^N w_i \{ y_i^{obs} - \frac{1}{c} y_i^{calc} \}^2, \tag{4.29}$$

where the sum is extended to all N data points of the diffraction patter, w_i is a statistical weight and c is a scale factor.

The convergence of equation 4.29 by means of non-linear least square algorithm needs an input of initial parameters that are not so far away from the solution [130]. In particular, it is necessary to provide an input of how many phases are expected in the pattern and their symmetry group. A good initial value of the lattice parameters is also required.

The quality of the refinement is usually assessed by figures of merit, such as the profile residual [131]

$$R_p = \sum_i^N \frac{|y_i^{obs} - y_i^{calc}|}{\sum_i^N y_i^{obs}} \times 100, \tag{4.30}$$

the weighted profile residual

$$R_{wp} = \sum_i^N w_i \frac{(y_i^{obs} - y_i^{calc})^2}{\sum_i^N w_i (y_i^{obs})^2} \times 100, \tag{4.31}$$

and the goodness of fit, which depends also on the number of refined parameter p,

$$\chi^2 = \sum_i^N \frac{(y_i^{obs} - y_i^{calc})^2}{n - p}. \tag{4.32}$$

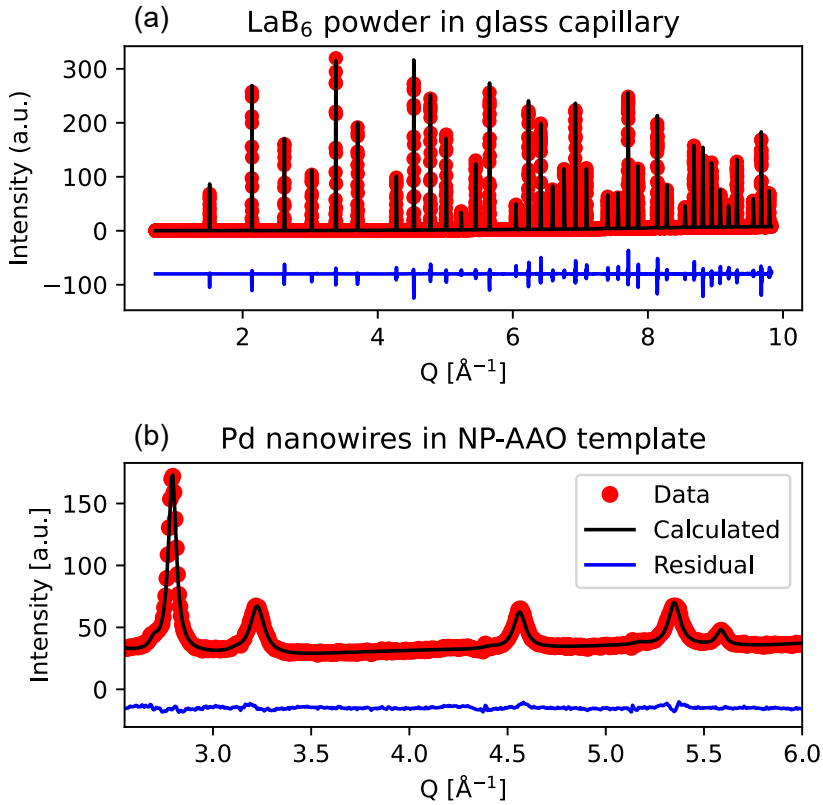

Figure 4.6: Rietveld refinement of a LaB_6 powder in a capillary (a), measured in the Debye-Scherrer geometry with an area detector (see Paper I); Rietveld refinement of Pd nanowires in NP-AAO template (b), measured in the grazing-incidence transmission geometry (see Paper V).

Fig. 4.6 shows two examples of Rietveld refinement. The data in Fig. 4.6 (a) was measured using a (2+3)-type surface diffractometer and an area detector, after vertically aligning a capillary of LaB_6 in the centre of the diffractometer. The measurement was performed using an x-ray beam energy of 20 keV, with a size of 100 μm $\times$ 300 μm (horizontal $\times$ vertical). The detector was scanned in the horizontal plane in an angular range from 4° to 60°. The data in Fig. 4.6 (b) was measured during the electrodeposition of Pd *in situ*. The difference between the observed intensity and the calculated model (the residual) is also reported in Fig. 4.6. In addition to the evaluation of the figures of merit like R_p, R_{wp} and χ^2, it is important to visually inspect the residual. A good Rietveld refinement should show fairly constant residues.

4.2 Small-angle x-ray scattering

The structure factor expressed as the Fourier Transform of the electron density in equation 4.11, suggests that any periodic structure gives rise to a diffraction pattern (assuming that the wavelength of the radiation used is smaller than the period of repetition). The limit of Bragg's law (equation 4.12) for $d \rightarrow \infty$ corresponds to infinitesimally small θ. Therefore, large-scale periodic structures (10-100 nm) lead to Bragg reflections at small θ angles (0.05-0.005° at 70 keV, or 0.18-0.018° at 20 keV). Small-angle x-ray scattering (SAXS) consists in detecting Bragg reflections and diffuse scattering in proximity of the transmitted x-ray beam, to learn about long-range order, size and morphology of a material [132, 133].

SAXS has been used widely in soft-matter applications to study the structure of macromolecular compounds such as polymers, colloids, surfactants, proteins, etc., loaded in glass capillaries [134]. For such applications, the transmission geometry is employed. However, SAXS can be performed at grazing-incidence geometry, to enable surface sensitivity (GISAXS). This is especially useful to investigate, e.g., arrays of nanomaterials on a substrate. The control over the penetration depth, discussed in §4.1.3, allows investigations of buried interfaces, too. When the chosen incidence angle is significantly above the critical angle of total external reflection, the system is better described by the grazing-incidence *transmission* geometry, which is the geometry used in Papers III, IV, V and VI.

4.2.1 Grazing-incidence transmission SAXS

The GISAXS patterns measured at angles close to the critical angle of total external reflection are subject to artefacts, described by the distorted wave Born approximation (DWBA) [135, 136]. Fig. 4.7 is a schematic of the contributions to a GISAXS pattern arising from a two-slab sample: scattering (a), reflection of the incident beam at the interface between the two slabs, followed by a scattering event (b), scattering followed by the reflection of the scattered light (c), reflection of the incident beam, followed by a scattering event and reflection of the scattered light (d). The DWBA helps to predict the scattering amplitude and look beyond the distortion of the GISAXS pat-

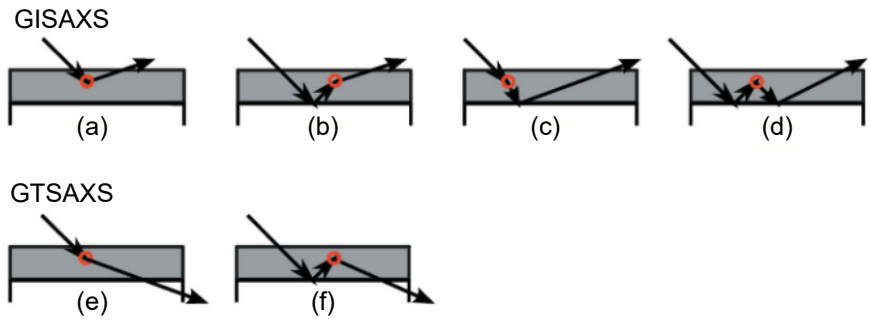

Figure 4.7: Schematic description of scattering events (represented by red dots) that occur in the GISAXS geometry, as described by the DWBA approximation [(a)-(d)], and in the GTSAXS geometry [(e) and (f)]. Reproduced from Ref. [139] with permission of the International Union of Crystallography.

terns, to retrieve information about the sample size and morphology. Some computer programs were developed to simulate and fit the GISAXS patterns affected by these distortions, such as *IsGISAXS* [137] and *BornAgain* [138].

A simpler approach consists in performing GISAXS at an incidence angle that is several times the critical angle, entering the grazing-incidence transmission SAXS (GTSAXS) regime [139]. In this geometry, the SAXS pattern is a contribution of scattering events or reflection at the two-slab interface followed by a scattering event [Fig. 4.7 (e) and (f)]. This is referred to as the Born approximation (BA), which describes conventional transmission SAXS data.

4.3 Electron microscopy

An electron beam is a kind of ionizing radiation that interacts with matter, transferring energy to tightly bound inner-shell electrons in atoms. There are several secondary processes caused by the interaction of electrons with matter, which are summarized in Fig. 4.8. An electron beam interacting with a specimen can generate secondary electrons, backscattered electrons, Auger electrons, characteristic and Bremsstrahlung x-rays. If high accelerating voltages are used and if the sample is sufficiently thin, the transmitted electron beam and scattering arising from the sample can be also detected. The general concepts summarized in this section are based on textbooks describing this

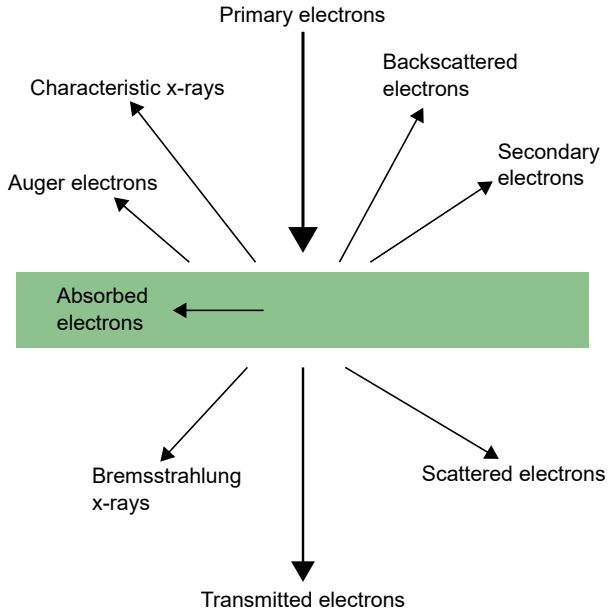

Figure 4.8: Schematic of the electron-matter interaction processes.

subject [140, 141].

4.3.1 Scanning electron microscopy (SEM)

Scanning electron microscopy (SEM) is primarily based on the detection of secondary electrons while systematically scanning the surface of the sample with a focused electron beam. Typically accelerating voltages of the primary electron beam are in the range 0.5-5 kV. The primary electrons penetrate into the material for some distance before they collide and transfer energy to the surrounding atoms. The interaction volume of the primary electrons is the region from which secondary electrons, backscattered electrons, characteristic x-rays and Auger electrons are generated. The penetration depth of this interaction is proportional to the accelerating voltage and inversely proportional to the atomic number of the atoms in the specimen observed, therefore the accelerating voltage can determine the surface sensitivity of the technique.

The secondary electrons are loosely bound to the atoms and escape from a region of a few nanometers from the surface. In most SEMs, an Everhalt-Thornley detector is

normally used to collect the secondary electrons, which consists of a scintillator (to which a potential of ca. +10 kV is applied), inside a Faraday cage (to which a potential of ca. +300 V is applied). The imaging of the specimen topography is conducted by correlating the history of the scan to the history of the detected secondary electron intensity.

Backscattered electrons can be used to visualize chemical contrast. While secondary electrons are subjected to inelastic collision and leave the sample surface in any direction with an energy smaller than 50 eV, backscattered electrons are elastically scattered towards the source. The probability of generating backscattered electrons is proportional to the cross-sectional area of the interaction with the atoms, hence the number of backscattered electrons is proportional to the atomic number Z. For this reason, backscattered electron imaging provides a chemical contrast between high-Z and low-Z atoms. However, since the backscattered electrons have an energy usually much higher than 50 eV, and therefore interact less with the surrounding atoms, they often originate from larger interaction volumes, reducing the surface sensitivity of the technique.

4.3.2 Focused ion beam (FIB)

Similar to SEM, focused ion beam (FIB) is a technique where a beam of Ga^+ ions is scanned on the specimen surface with typical accelerating voltages of 10-30 kV [142]. At such potential, the Ga^+ ions sputter the surface of the material, causing the ejection of ions or neutral atoms. FIB is mostly used for systematical milling of the material, rather than for imaging purposes. FIB milling yields some neat cross-sections which are well-suited for the observation and the analysis of buried or encapsulated interfaces. Often, to protect the specimen from excessive sputtering of material, a strip of Pt is deposited by operating the FIB while a gaseous injection system (GIS) introduces Pt in the chamber. Fig. 4.9 (a) is a schematic representation of the arrangements of the operating conditions of a typical FIB-SEM. In this thesis work, an SEM equipped with a FIB has been used to mill cross-sectional regions of NP-AAO after the electrodeposition of metals, in order to assess the result of the electrodeposition in terms of morphology of the material and aspect ratio of the fabricated nanowires, such as

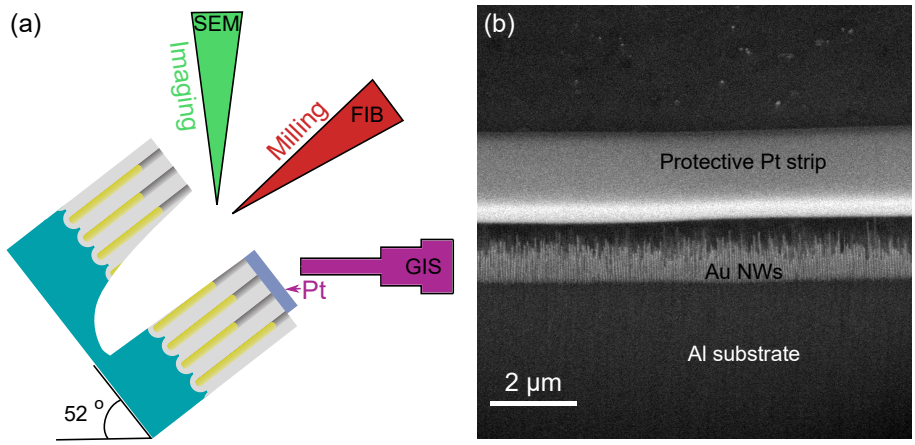

Figure 4.9: (a) Schematic of the operating conditions of a FIB-SEM, (b) a typical cross-sectional view of Au nanowires in NP-AAO, obtained by FIB milling (see Paper IV).

those in Fig. 4.9 (b).

4.3.3 Transmission electron microscopy (TEM)

In transmission electron microscopy (TEM), the primary beam goes through a thin sample, then the transmitted beam goes through a system of lenses and apertures in order to project a magnified image of the specimen onto a fluorescent screen. Since the accelerating voltages are high (200-300 kV), the de Broglie wavelength of the electrons is significantly small and high resolutions are possible. A schematic of a typical TEM setup is shown in Fig. 4.11. In addition, by inserting an aperture in one of the image planes of the imaging lens, it is possible to perform selected-area electron diffraction (SAED). Similarly to x-ray diffraction, electron diffraction allows us to extract structural information from the investigated specimen. In contrast with x-ray diffraction, (i) the structural information is not averaged over a large area of the sample, but it arises from the relatively small area selected and (ii) the kinematical approximation no longer holds and multiple, dynamical scattering must be considered.

In this thesis, TEM and SAED have been used to characterize the Au and Pd nanostructures electrodeposited in NP-AAO. Fig. 4.10 shows a typical TEM image of some Au nanoparticles and a SAED pattern, arising from the fcc structure of Au.

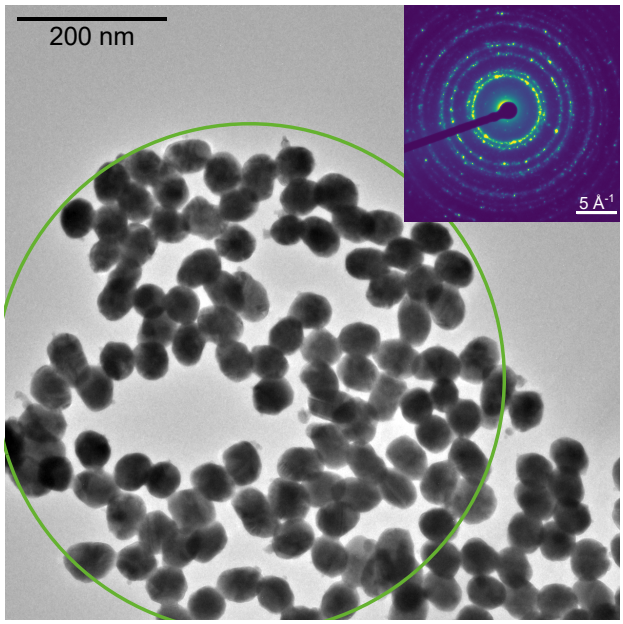

Figure 4.10: TEM micrograph of Au nanoparticles grown in NP-AAO. The SAED pattern in the inset arises from the circled selected area (see Paper IV).

4.4 X-ray fluorescence

X-ray photons with sufficient energy can interact with matter causing the photoemission of core electrons in an atom [118]. This can cause vacancies in the electron orbitals, as shown in Fig. 4.12 (a). These vacancies can be refilled by electrons in outer-shell orbitals, causing the release of energy in the form of a photon. The energy of the emitted photon equals the energy difference between the orbitals involved in the transition, as shown in Fig. 4.12 (b). This phenomenon is called x-ray fluorescence (XRF). In XRF, the Siegbahn notation is often used to denominate transitions occurring from the various electronic shells [143]. For instance, transitions from L to K shells are called K_α, while transitions from M to K shells are called K_β. Silicon drift detectors (SDD) are normally used to detect XRF spectra, or regions of interest around a particular emission line.

X-rays are not the only ionizing radiation that causes emission of characteristic lines. In fact, XRF can be stimulated by electron beams. For this reason, SEMs and TEMs are often equipped with SDDs, to learn about the chemistry of the investigated mate-

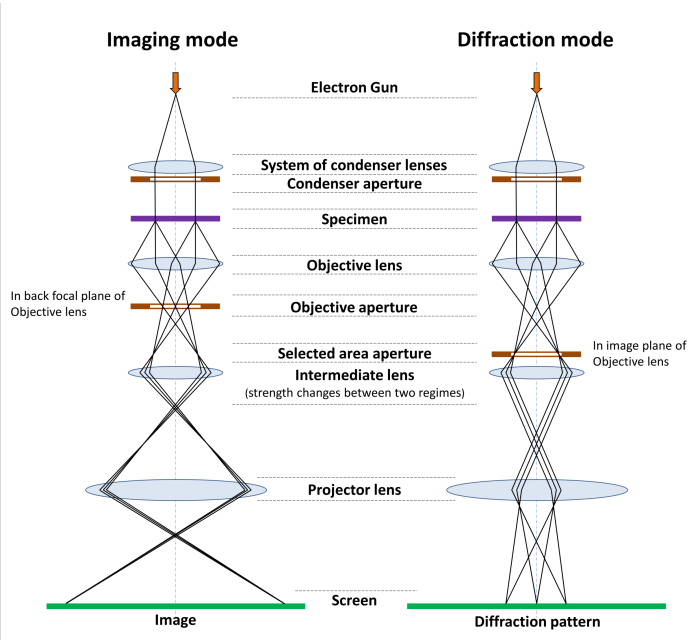

Figure 4.11: Schematic representation of the TEM in imaging and diffraction mode. (Image credits: Eric Kvaalen, CC BY-SA 4.0)

rial. In the field of electron microscopy, XRF is often referred to as energy dispersive x-ray spectroscopy (EDS or EDX).

4.5 Two-dimensional surface optical reflectance (2D-SOR)

Two-dimensional surface optical reflectance (2D-SOR) is a technique where the intensity of optical light, reflected by a surface, is imaged by a camera through a microscope. Although traditional SOR was measured with point detectors, recent advances of the technique enabled observation of the reflecting surface with spatial resolution [144–146].

Fig. 1 of Paper VII shows a schematic of a 2D-SOR setup used to measure the reflectance from a specimen surface under electrochemical conditions. The light from a LED with a wavelength of 660 nm is reflected by a mirror beam splitter and focused on the sample surface. The optical path goes through a system of lenses and towards a camera. With this setup it is possible to measure optical reflectance with a spatial

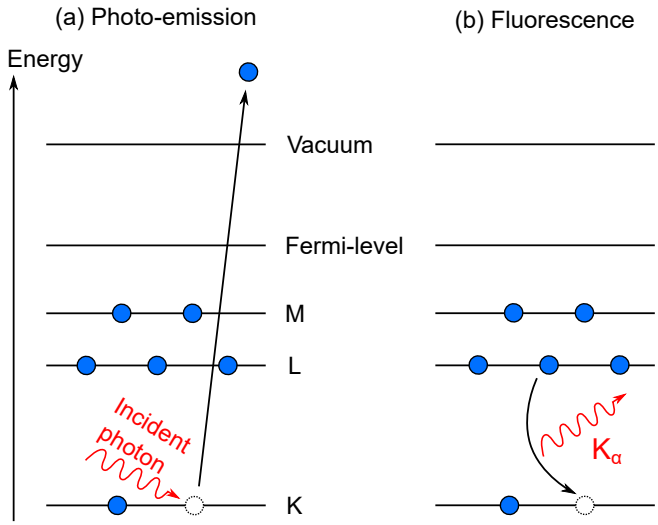

Figure 4.12: Schematic energy level diagram of an atom during fluorescent x-ray emission. (a) A photon is absorbed by the atom and an electron is photo-emitted, leaving a vacancy behind. (b) The vacancy is refilled by electrons in outer shells, stimulating the fluorescent emission.

resolution that depends on the magnification of the microscope.

In the 2D-SOR setup shown here, the incident light is normal to the surface. In this geometry, the Fresnel reflectance coefficient is independent of the light polarization and can be expressed as [147]:

$$R = \left| \frac{n_1 - n_2}{n_1 + n_2} \right|^2, \tag{4.33}$$

where n_1 is the refractive index of the medium (in this case aqueous electrolyte) and n_2 is the refractive index of the investigated surface.

Since imaging of the pores is not possible with a conventional optical microscope, the measured reflectance of each pixel arises from an averaging over regions of approximately 5 μm in size (the spatial resolution of a typical 2D-SOR frame). The existence of such averaging effect is supported by the Maxwell-Garnett approximation for the effective dielectric constant of composite materials [148, 149]. This theory predicts that the dielectric constant of a membrane of NP-AAO containing metal nanoparticles, has a dielectric constant ϵ expressed as

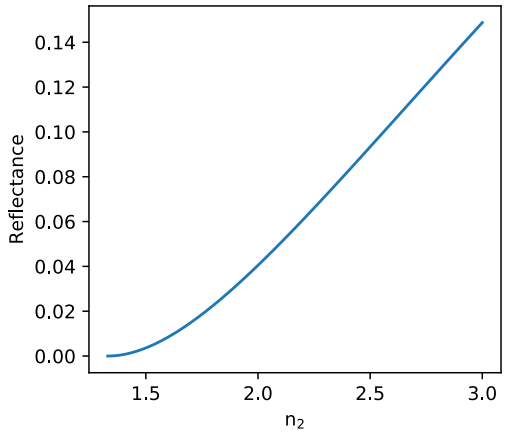

Figure 4.13: Simulation of the reflectance of as a function of the refractive index of the reflecting medium n_2.

$$\frac{\epsilon - \epsilon_0}{\epsilon + k\epsilon_0} = f_m \frac{\epsilon_m - \epsilon_0}{\epsilon_m + \epsilon_0}, \tag{4.34}$$

where ϵ_0 is the dielectric constant of the membrane, ϵ_m is the dielectric constant of the metal, k is a parameter dependent on the shape of the nanoparticles and f_m is the volume fraction of the membrane occupied by the nanowires. The dielectric constant of the material is related to the refractive index and therefore to the reflectance through the proportionality $n \propto \sqrt{\epsilon}$. Fig. 4.13 shows a simulation of the reflectance as a function of the refractive index of the reflecting medium n_2, calculated using equation 4.33 substituting n_1 with the refractive index of water n_{H_2O}=1.333. Here, the reflectance increases as a function of the refractive index of the reflecting surface. Therefore, as the pores are filled and the average refractive index of the material increases due to the metal growing in the pores, one would expect an increase in the overall 2D-SOR signal.

However, the 2D-SOR images collected during the electrodeposition of Au and Pd, shown in Fig. 4.14 (a) and (b), reveal a decrease in the reflected intensity. This suggests that reflection is not the only light/matter interaction occurring. Although the origin of the reflectance decay is not fully understood yet, it could be explained by plasmon absorption in the growing nanowires. In fact, existing studies on Au nanorods encapsulated in NP-AAO, have shown an overall increase in the UV/Vis absorbance spectra

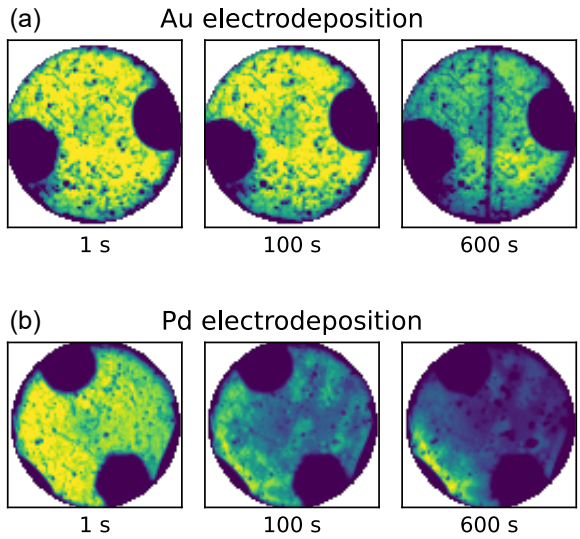

Figure 4.14: 2D-SOR images collected during the electrodeposition of Au (a) and (Pd). In (a), a vertical streak progressively appears, due to exposure to a high-energy x-ray beam during the measurement.

as a function of the nanorods aspect ratio [150]. Therefore, one could speculate that the light illuminating the sample surface is incrementally attenuated as the nanorods grow. However, this hypothesis could only be verified by using spectroscopy, which is beyond the purpose and potentiality of a 2D-SOR measurement.

Chapter 5

Summary and Outlook

Part of this thesis consisted in establishing a reproducible protocol for the electrodeposition of Au and Pd into NP-AAO templates. Using the method proposed, ordered arrays of nanowires embedded in NP-AAO were fabricated. In order to learn about the structure of the fabricated nanowires, *ex situ* GIXRD was used. Synchrotron x-ray diffraction with a (2+3)-type surface diffractometer, equipped with an area detector was used for the structural evaluation. A protocol for the data reduction was established to obtain one-dimensional powder diffraction patterns from such diffractometer. Thanks to the rotational degrees of freedom of the diffractometer detector arm, we could measure Au and Pd nanowires in NP-AAO *ex situ* and learn about the strain anisotropy of Au and Pd nanowires electrodeposited in NP-AAO. Compared to the theoretical bulk values, the lattice constant of both Au and Pd was slightly smaller in the direction of confinement (i.e., the the horizontal direction) and slightly higher in the direction of growth (i.e., the vertical direction).

For a better understanding of the structure-function relation of the Au and Pd nanowires, we explored their growth *in situ*. During such measurements, conducted during the electrodeposition of Pd, strain variations and phase transitions were observed. On the other hand, during the growth of Au nanowires, a time-dependent strain anisotropy was detected. These aspects of the growth were unnoticeable in *ex situ* measurements and underline the importance of time-resolved *in situ* measurements.

An electrochemical flow-cell, specifically designed for x-ray measurements, was used to perform *in situ* electrochemistry at synchrotron facilities. A part of this thesis work consisted in combining such cell with 2D-SOR, to obtain a versatile setup to monitor electrochemical processes in real time. Such setup is easily transportable and has been used in combination with synchrotron measurements.

In addition to XRD, we followed *in situ* the electrodeposition of Au and Pd in NP-AAO templates by using GTSAXS, which is sensitive to the long range order (50-500 nm) of the nano-porous domains. Such measurements revealed information on dynamics, time-scale and homogeneity of the pore filling.

I Quantitative powder diffraction using a (2+3) surface diffractometer and an area detector

Although originally designed for surface x-ray diffraction, (2+3)-type diffractometers can be used to measure powders, textured materials and interfaces. However, extracting quantitative information from a scanning rotating area detector is not a trivial operation. In order to extract a powder diffraction pattern from a stack of detector images, a data reduction protocol was established. It consists in angle calculations that assign a diffraction angle to each pixel of each detector image. An intensity binning operation, based on the pixel-angle assignment yields one-dimensional diffraction patterns, perhaps more familiar to the readers in the powder diffraction field. As a proof of principle, we measured a standard reference material (LaB_6), processed the data using the presented angle calculations, applied the intensity correction factors and performed Rietveld refinement to extract quantitative information.

II Electrochemical Fabrication and Characterization of Palladium Nanowires in Nanoporous Alumina Templates

In this paper, ordered arrays of Pd nanowires were fabricated by electrodeposition in NP-AAO. The templates were prepared in different conditions of anodizing solution and anodizing potential. Both were treated by means of electrochemical barrier layer thinning. The effect of such template preparation method on the morphology of

the nanowires was studied by FIB-SEM. Furthermore, the diffractometer described in Paper I was used to characterize the nanowires *ex situ* by means of GIXRD. This technique revealed anisotropies in crystallite size and lattice parameters, attributed to growth in confined environment.

III *In situ* scanning x-ray diffraction reveals strain variations in electrochemically grown nanowires

The method presented in Paper II to fabricate Pd nanowires has been used *in situ* growth studies, by means XRD with a submicron hard x-ray beam. Space-resolved tensile strain variations as a function of pore depth were detected, revealing higher strain in proximity of the branched nanowires bottom.

IV Templated electrodeposition as a scalable and surfactant-free approach to the synthesis of Au nanoparticles with tunable aspect ratios

In this paper, ordered arrays of Au nanostructures were fabricated by electrodeposition in NP-AAO. The templates were prepared by anodizing the aluminum in H_2SO_4 and treated by either pore widening or electrochemical barrier layer thinning. FIB-SEM was used to study the effect that the templates have on the morphology and the aspect ratio of the nanomaterials. Similarly to Paper II, we detected anisotropies in crystallite size and lattice parameter, which depend on the template pore size.

V *In situ* hydride breathing during the electrochemical growth of Pd nanowires

In this work, high-energy SAXS and WAXS were used to characterize the growth of Pd nanowires *in situ*. The key finding is that the nanomaterials grow as Pd hydride, due to the presence of hydrogen evolving at the metal/electrolyte interface. Furthermore, alternating sequences of electrodeposition to sequences of rest caused phase transitions from β- to α-phase Pd hydride.

VI Anisotropic strain variations during the confined growth of Au nanowires

In this short communication manuscript, the electrochemical growth of Au nanowires in NP-AAO was followed *in situ* using the same setup as in Paper V. By using WAXS, the evolution of the direction-dependent lattice parameter was monitored. Small strain fluctuations in the direction of growth were found by alternating sequences of electrodeposition with sequences of rest, which revealed that the electric field might influence the interatomic distances of the nanomaterials during their formation. At the same time, SAXS revealed insights on heterogeneous pore filling dynamics.

VII An electrochemical cell for 2-dimensional surface optical reflectance during anodization and cyclic voltammetry

The combination of electrochemical flow-cell with 2D-SOR is a powerful tool that can be used for surface studies under electrochemical conditions. A demonstration of such setup is here shown for different electrodes, under oxidising and reducing conditions.

Outlook

The Au and Pd arrays of nanowires fabricated in the course of this thesis work, could be used in future studies as devices under *operando* conditions. For instance, arrays of Pd nanowires in NP-AAO could be used as the working electrode in an electrochemical flow-cell, to initiate Pd hydride phase transitions and observe the dynamics of hydrogen absorption and desorption. This system is potentially a good framework for the understanding of the stability of Pd hydride nanostructures, towards applications in hydrogen storage and sensing. In this regard, the behaviour of the Pd hydride *breathing* could be investigated as a function of the electrolyte pH, since there are two possible pathways of hydrogen absorption: upon dissociation of H_2 and from H^+. Additionally, the hydride breathing could be observed *in situ* as a function of electrolyte temperature to learn about the diffusivity of hydrogen in the nanowires under

electrochemical conditions. Another aspect that should be investigated is weather or not presence of a x-ray beam has in influence on the hydride formation.

Ideally, it should be possible to combine Pd with other alloying metals such as Ag, to increase the resistance to embrittlement, reduce the cost and improve the material performance [151, 152]. Pd can be potentially combined with other metals to obtain metal nanowire heterestructure or multi-segmented nanowires. For instance, one could deposit segments of metals with hydriding properties, such as V, Fe and MgO, and deposit a top segment of Pd. This approach is inspired by studies making use of multi-layered materials, where a top layer of Pd is deposited to facilitate the reversible hydrogen absorption and desorption [153].

The Au nanostructures fabricated in this thesis work have potential applications in many fields of science. It should be emphasized that the order of the nanowire arrays is based on the self-organized honeycomb structure of NP-AAO. Since large areas of Al can be anodized at once, the nanowire fabrication should be easily scalable, for industrial purposes. Furthermore, both the Au and the Pd nanostructures were fabricated in absence of surfactants or capping agents and are thus readily available for applications, whereas in some colloidal synthesis methods a de-capping stage is necessary. Although the nanostructures are encapsulated in NP-AAO, the template can be selectively dissolved to expose the surface of the nanostructures for applications where the availability of surface sites is relevant, e.g., catalysis.

Finally, it has been shown that the growth in confined environments leads to a size-dependent anisotropic deformation of the unit cell. This is potentially a useful finding in fields such as strain engineering, catalysis and devices design. However, it is still not clear what the origin of the stress that causes such deformation is and if the strain is released upon selective dissolution of the NP-AAO template. An *in situ* observation of the lattice parameter could be performed to find this out, while releasing the nanowires in solution.

References

[1] Richard P. Feynman. There's plenty of room at the bottom. In *American Physical Society Meeting in Pasadena CA*, 1959.

[2] Vinod K. Sangwan and Mark C. Hersam. Neuromorphic nanoelectronic materials. *Nature Nanotechnology*, 15(7):517–528, Jul 2020. ISSN 1748-3395. doi: 10.1038/s41565-020-0647-z. URL https://doi.org/10.1038/s41565-020-0647-z.

[3] Xiaoli Zhao, Hong Jin, Jiayao Liu, Jiale Chao, Tingyi Liu, Han Zhang, Gang Wang, Wenhao Lyu, Swelm Wageh, Omar A. Al-Hartomy, Abdullah G. Al-Sehemi, Bo Fu, and Han Zhang. Integration and applications of nanomaterials for ultrafast photonics. *Laser & Photonics Reviews*, n/a(n/a):2200386, 2022. doi: https://doi.org/10.1002/lpor.202200386. URL https://onlinelibrary.wiley.com/doi/abs/10.1002/lpor.202200386.

[4] Qifeng Zhang, Evan Uchaker, Stephanie L. Candelaria, and Guozhong Cao. Nanomaterials for energy conversion and storage. *Chem. Soc. Rev.*, 42:3127–3171, 2013. doi: 10.1039/C3CS00009E. URL http://dx.doi.org/10.1039/C3CS00009E.

[5] Pooyan Makvandi, Chen-yu Wang, Ehsan Nazarzadeh Zare, Assunta Borzacchiello, Li-na Niu, and Franklin R. Tay. Metal-based nanomaterials in biomedical applications: Antimicrobial activity and cytotoxicity aspects. *Advanced Functional Materials*, 30(22):1910021, 2020. doi: https://doi.org/10.1002/adfm.201910021. URL https://onlinelibrary.wiley.com/doi/abs/10.1002/adfm.201910021.

[6] Liberato Manna, Erik C. Scher, and Armand P. Alivisatos. Shape control of colloidal semiconductor nanocrystals. *Journal of Cluster Science*, 13(4):521–532, Dec 2002. ISSN 1572-8862. doi: 10.1023/A:1021175612112. URL https://doi.org/10.1023/A:1021175612112.

[7] Xiaogang Peng, Liberato Manna, Weidong Yang, Juanita Wickham, Erik Scher, Andreas Kadavanich, and Armand P. Alivisatos. Shape control of CdSe nanocrystals. *Nature*, 404(6773):59–61, Mar 2000. ISSN 1476-4687. doi: 10.1038/35003535. URL https://doi.org/10.1038/35003535.

[8] V. A. Fonoberov, E. P. Pokatilov, and A. A. Balandin. Exciton states and optical transitions in colloidal CdS quantum dots: Shape and dielectric mismatch effects. *Phys. Rev. B*, 66:085310, Aug 2002. doi: 10.1103/PhysRevB.66.085310. URL https://link.aps.org/doi/10.1103/PhysRevB.66.085310.

[9] William E. Buhro and Vicki L. Colvin. Shape matters. *Nature Materials*, 2(3): 138–139, Mar 2003. ISSN 1476-4660. doi: 10.1038/nmat844. URL https://doi.org/10.1038/nmat844.

[10] A. N. Goldstein, C. M. Echer, and A. P. Alivisatos. Melting in semiconductor nanocrystals. *Science*, 256(5062):1425–1427, 1992. doi: 10.1126/science.256.5062.1425. URL https://www.science.org/doi/abs/10.1126/science.256.5062.1425.

[11] Kevin F. Peters, Jerome B. Cohen, and Yip-Wah Chung. Melting of Pb nanocrystals. *Phys. Rev. B*, 57:13430–13438, Jun 1998. doi: 10.1103/PhysRevB.57.13430. URL https://link.aps.org/doi/10.1103/PhysRevB.57.13430.

[12] Philomena Schlexer, Anton Bay Andersen, Bela Sebok, Ib Chorkendorff, Jakob Schiøtz, and Thomas W. Hansen. Size-dependence of the melting temperature of individual Au nanoparticles. *Particle & Particle Systems Characterization*, 36 (3):1800480, 2019. doi: https://doi.org/10.1002/ppsc.201800480. URL https://onlinelibrary.wiley.com/doi/abs/10.1002/ppsc.201800480.

[13] Atta Ul Haq, Sadegh Askari, Anna McLister, Sean Rawlinson, James Davis, Supriya Chakrabarti, Vladimir Svrcek, Paul Maguire, Pagona Papakonstanti-

nou, and Davide Mariotti. Size-dependent stability of ultra-small α-/β-phase tin nanocrystals synthesized by microplasma. *Nature Communications*, 10(1): 817, Feb 2019. ISSN 2041-1723. doi: 10.1038/s41467-019-08661-9. URL https://doi.org/10.1038/s41467-019-08661-9.

[14] James R. Heath. Covalency in semiconductor quantum dots. *Chem. Soc. Rev.*, 27:65–71, 1998. doi: 10.1039/A827065Z. URL http://dx.doi.org/10.1039/A827065Z.

[15] Susie Eustis and Mostafa A. El-Sayed. Why gold nanoparticles are more precious than pretty gold: Noble metal surface plasmon resonance and its enhancement of the radiative and nonradiative properties of nanocrystals of different shapes. *Chem. Soc. Rev.*, 35:209–217, 2006. doi: 10.1039/B514191E. URL http://dx.doi.org/10.1039/B514191E.

[16] Vincenzo Amendola, Roberto Pilot, Marco Frasconi, Onofrio M. Maragò, and Maria Antonia Iatì. Surface plasmon resonance in gold nanoparticles: a review. *Journal of Physics: Condensed Matter*, 29(20):203002, apr 2017. doi: 10.1088/1361-648X/aa60f3. URL https://dx.doi.org/10.1088/1361-648X/aa60f3.

[17] Sarah De Marchi, Sara Núñez-Sánchez, Gustavo Bodelón, Jorge Pérez-Juste, and Isabel Pastoriza-Santos. Pd nanoparticles as a plasmonic material: synthesis, optical properties and applications. *Nanoscale*, 12:23424–23443, 2020. doi: 10.1039/D0NR06270G. URL http://dx.doi.org/10.1039/D0NR06270G.

[18] M.S. Chen and D.W. Goodman. Structure–activity relationships in supported Au catalysts. *Catalysis Today*, 111(1):22–33, 2006. ISSN 0920-5861. doi: https://doi.org/10.1016/j.cattod.2005.10.007. URL https://www.sciencedirect.com/science/article/pii/S0920586105007029. Frontiers in Catalysis: A Molecular View of Industrial Catalysis.

[19] Britt Hvolbæk, Ton V.W. Janssens, Bjerne S. Clausen, Hanne Falsig, Claus H. Christensen, and Jens K. Nørskov. Catalytic activity of Au nanoparticles. *Nano Today*, 2(4):14–18, 2007. ISSN 1748-0132. doi: https://doi.org/10.

1016/S1748-0132(07)70113-5. URL https://www.sciencedirect.com/science/article/pii/S1748013207701135.

[20] Diego J. Gavia and Young-Seok Shon. Catalytic properties of unsupported palladium nanoparticle surfaces capped with small organic ligands. *ChemCatChem*, 7(6):892–900, 2015. doi: https://doi.org/10.1002/cctc.201402865. URL https://chemistry-europe.onlinelibrary.wiley.com/doi/abs/10.1002/cctc.201402865.

[21] Mahmoud Nasrollahzadeh, Mohaddeseh Sajjadi, Mohammadreza Shokouhimehr, and Rajender S. Varma. Recent developments in palladium (nano)catalysts supported on polymers for selective and sustainable oxidation processes. *Coordination Chemistry Reviews*, 397:54–75, 2019. ISSN 0010-8545. doi: https://doi.org/10.1016/j.ccr.2019.06.010. URL https://www.sciencedirect.com/science/article/pii/S0010854519301389.

[22] Hui Xu, Hongyuan Shang, Cheng Wang, and Yukou Du. Ultrafine Pt -based nanowires for advanced catalysis. *Advanced Functional Materials*, 30(28): 2000793, 2020. doi: https://doi.org/10.1002/adfm.202000793. URL https://onlinelibrary.wiley.com/doi/abs/10.1002/adfm.202000793.

[23] Rajesh Sardar, Alison M. Funston, Paul Mulvaney, and Royce W. Murray. Gold nanoparticles: Past, present, and future. *Langmuir*, 25(24):13840–13851, Dec 2009. ISSN 0743-7463. doi: 10.1021/la9019475. URL https://doi.org/10.1021/la9019475.

[24] Oxana V. Kharissova, H.V. Rasika Dias, Boris I. Kharisov, Betsabee Olvera Pérez, and Victor M. Jiménez Pérez. The greener synthesis of nanoparticles. *Trends in Biotechnology*, 31(4):240–248, 2013. ISSN 0167-7799. doi: https://doi.org/10.1016/j.tibtech.2013.01.003. URL https://www.sciencedirect.com/science/article/pii/S0167779913000152.

[25] Warren CW Chan. *Bio-applications of Nanoparticles*, volume 620. Springer Science & Business Media, 2009.

[26] Dongguo Li, Chao Wang, Dusan Tripkovic, Shouheng Sun, Nenad M. Markovic, and Vojislav R. Stamenkovic. Surfactant removal for colloidal

nanoparticles from solution synthesis: The effect on catalytic performance. *ACS Catalysis*, 2(7):1358–1362, Jul 2012. doi: 10.1021/cs300219j. URL https://doi.org/10.1021/cs300219j.

[27] Yadian Xie, Duygu Kocaefe, Chunying Chen, and Yasar Kocaefe. Review of research on template methods in preparation of nanomaterials. *Journal of Nanomaterials*, 2016:2302595, Jul 2016. ISSN 1687-4110. doi: 10.1155/2016/2302595. URL https://doi.org/10.1155/2016/2302595.

[28] K. Nielsch, F. Müller, A.-P. Li, and U. Gösele. Uniform nickel deposition into ordered alumina pores by pulsed electrodeposition. *Advanced Materials*, 12(8):582–586, 2000. doi: https://doi.org/10.1002/(SICI)1521-4095(200004)12:8<582::AID-ADMA582>3.0.CO;2-3.

[29] Kornelius Nielsch, Jinsub Choi, Kathrin Schwirn, Ralf B. Wehrspohn, and Ulrich Gösele. Self-ordering regimes of porous alumina: the 10 porosity rule. *Nano Letters*, 2(7):677–680, Jul 2002. ISSN 1530-6984. doi: 10.1021/nl025537k. URL https://doi.org/10.1021/nl025537k.

[30] Debasis Bera, Suresh C. Kuiry, and Sudipta Seal. Synthesis of nanostructured materials using template-assisted electrodeposition. *JOM*, 56(1):49–53, Jan 2004. ISSN 1543-1851. doi: 10.1007/s11837-004-0273-5. URL https://doi.org/10.1007/s11837-004-0273-5.

[31] Xiu-Yu Sun, Fa-Qiang Xu, Zong-Mu Li, and Wen-Hua Zhang. Cyclic voltammetry for the fabrication of high dense silver nanowire arrays with the assistance of AAO template. *Materials Chemistry and Physics*, 90(1):69–72, 2005. ISSN 0254-0584. doi: https://doi.org/10.1016/j.matchemphys.2004.10.007. URL https://www.sciencedirect.com/science/article/pii/S0254058404004869.

[32] Kyungtae Kim, Moonjung Kim, and Sung M. Cho. Pulsed electrodeposition of palladium nanowire arrays using AAO template. *Materials Chemistry and Physics*, 96(2):278–282, 2006. ISSN 0254-0584. doi: https://doi.org/10.1016/j.matchemphys.2005.07.013. URL https://www.sciencedirect.com/science/article/pii/S0254058405004566.

[33] Nevin Taşaltın, Sadullah Öztürk, Necmettin Kılınç, Hayrettin Yüzer, and ZaferZiya Öztürk. Fabrication of vertically aligned Pd nanowire array in AAO template by electrodeposition using neutral electrolyte. *Nanoscale Research Letters*, 5(7):1137, May 2010. ISSN 1556-276X. doi: 10.1007/s11671-010-9616-z. URL https://doi.org/10.1007/s11671-010-9616-z.

[34] U. S. Mohanty. Electrodeposition: a versatile and inexpensive tool for the synthesis of nanoparticles, nanorods, nanowires, and nanoclusters of metals. *Journal of Applied Electrochemistry*, 41(3):257–270, Mar 2011. ISSN 1572-8838. doi: 10.1007/s10800-010-0234-3. URL https://doi.org/10.1007/s10800-010-0234-3.

[35] M. Hernández-Vélez. Nanowires and 1d arrays fabrication: An overview. *Thin Solid Films*, 495(1):51–63, 2006. ISSN 0040-6090. doi: https://doi.org/10.1016/j.tsf.2005.08.331. URL https://www.sciencedirect.com/science/article/pii/S0040609005014033. EMRS 2005 Symposium E.

[36] Wan Young Jang, N. N. Kulkarni, C. K. Shih, and Zhen Yao. Electrical characterization of individual carbon nanotubes grown in nanoporous anodic alumina templates. *Applied Physics Letters*, 84(7):1177–1179, 2004. doi: 10.1063/1.1646752. URL https://doi.org/10.1063/1.1646752.

[37] A. Johansson, J. Lu, J.-O. Carlsson, and M. Boman. Deposition of palladium nanoparticles on the pore walls of anodic alumina using sequential electroless deposition. *Journal of Applied Physics*, 96(9):5189–5194, 2004. doi: 10.1063/1.1788843. URL https://doi.org/10.1063/1.1788843.

[38] Chienwen Huang, Jiechao Jiang, Mingyu Lu, Li Sun, Efstathios I. Meletis, and Yaowu Hao. Capturing electrochemically evolved nanobubbles by electroless deposition: A facile route to the synthesis of hollow nanoparticles. *Nano Letters*, 9(12):4297–4301, Dec 2009. ISSN 1530-6984. doi: 10.1021/nl902529y. URL https://doi.org/10.1021/nl902529y.

[39] P. Ramana Reddy, K.M. Ajith, and N.K. Udayashankar. Structural and optical analysis of silver nanoparticles grown on porous anodic alumina mem-

branes by electro-less deposition. *Materials Today: Proceedings*, 19:2633–2638, 2019. ISSN 2214-7853. doi: https://doi.org/10.1016/j.matpr.2019.10.109. URL https://www.sciencedirect.com/science/article/pii/S2214785319336181. National conference on Functionality of Advanced Materials.

[40] Jian Li, Mrityunjay Kothari, S. Chockalingam, Thomas Henzel, Qiuting Zhang, Xuanhe Li, Jing Yan, and Tal Cohen. Nonlinear inclusion theory with application to the growth and morphogenesis of a confined body. *Journal of the Mechanics and Physics of Solids*, 159:104709, February 2022. ISSN 00225096. doi: 10.1016/j.jmps.2021.104709. URL https://linkinghub.elsevier.com/retrieve/pii/S0022509621003239.

[41] P. Sharma and S. Ganti. Size-dependent eshelby's tensor for embedded nano-inclusions incorporating surface/interface energies. *Journal of Applied Mechanics*, 71(5):663–671, September 2004. ISSN 0021-8936, 1528-9036. doi: 10.1115/1.1781177. URL https://asmedigitalcollection.asme.org/appliedmechanics/article/71/5/663/471562/SizeDependent-Eshelbys-Tensor-for-Embedded.

[42] Yezeng Huang, Peng Yan, Junbo Wang, Leiting Dong, and Satya N. Atluri. Eshelby tensors and overall properties of nano-composites considering both interface stretching and bending effects. *Journal of Micromechanics and Molecular Physics*, pages 1–11, January 2022. ISSN 2424-9130, 2424-9149. doi: 10.1142/S2424913021420091. URL https://www.worldscientific.com/doi/abs/10.1142/S2424913021420091.

[43] Mingchuan Luo and Shaojun Guo. Strain-controlled electrocatalysis on multimetallic nanomaterials. *Nature Reviews Materials*, 2(11):17059, November 2017. ISSN 2058-8437. doi: 10.1038/natrevmats.2017.59. URL http://www.nature.com/articles/natrevmats201759.

[44] A.G.N. Sofiah, M. Samykano, K. Kadirgama, R.V. Mohan, and N.A.C. Lah. Metallic nanowires: Mechanical properties – Theory and experiment. *Applied Materials Today*, 11:320–337, 2018. ISSN 2352-9407. doi: https://

doi.org/10.1016/j.apmt.2018.03.004. URL https://www.sciencedirect.com/science/article/pii/S235294071830060X.

[45] J. Evertsson, F. Bertram, F. Zhang, L. Rullik, L.R. Merte, M. Shipilin, M. Soldemo, S. Ahmadi, N. Vinogradov, F. Carlà, J. Weissenrieder, M. Göthelid, J. Pan, A. Mikkelsen, J.-O. Nilsson, and E. Lundgren. The thickness of native oxides on aluminum alloys and single crystals. *Applied Surface Science*, 349: 826–832, 2015. ISSN 0169-4332. doi: https://doi.org/10.1016/j.apsusc.2015.05.043. URL https://www.sciencedirect.com/science/article/pii/S0169433215011617.

[46] H. Buff. Ueber das electrische verhalten des aluminiums. *Justus Liebigs Annalen der Chemie*, 102(3):265–284, 1857. doi: https://doi.org/10.1002/jlac.18571020302. URL https://chemistry-europe.onlinelibrary.wiley.com/doi/abs/10.1002/jlac.18571020302.

[47] J Wn Diggle, Thomas C Downie, and CW Goulding. Anodic oxide films on aluminum. *Chemical Reviews*, 69(3):365–405, 1969.

[48] G.E Thompson. Porous anodic alumina: fabrication, characterization and applications. *Thin Solid Films*, 297(1):192–201, 1997. ISSN 0040-6090. doi: https://doi.org/10.1016/S0040-6090(96)09440-0. URL https://www.sciencedirect.com/science/article/pii/S0040609096094400.

[49] Hideki Masuda and Kenji Fukuda. Ordered metal nanohole arrays made by a two-step replication of honeycomb structures of anodic alumina. *Science*, 268(5216):1466–1468, 1995. doi: 10.1126/science.268.5216.1466. URL https://www.science.org/doi/abs/10.1126/science.268.5216.1466.

[50] Hideki Masuda, Fumio Hasegwa, and Sachiko Ono. Self-ordering of cell arrangement of anodic porous alumina formed in sulfuric acid solution. *Journal of The Electrochemical Society*, 144(5):L127–L130, may 1997. doi: 10.1149/1.1837634. URL https://doi.org/10.1149/1.1837634.

[51] J. P. O'Sullivan, G. C. Wood, and Nevill Francis Mott. The morphology and mechanism of formation of porous anodic films on aluminium. *Pro-*

ceedings of the Royal Society of London. A. Mathematical and Physical Sciences, 317(1531):511–543, 1970. doi: 10.1098/rspa.1970.0129. URL https://royalsocietypublishing.org/doi/abs/10.1098/rspa.1970.0129.

[52] Woo Lee and Sang-Joon Park. Porous anodic aluminum oxide: Anodization and templated synthesis of functional nanostructures. *Chemical Reviews*, 114 (15):7487–7556, Aug 2014. ISSN 0009-2665. doi: 10.1021/cr500002z. URL https://doi.org/10.1021/cr500002z.

[53] J. A. González, V. López, A. Bautista, E. Otero, and X. R. Nóvoa. Characterization of porous aluminium oxide films from a.c. impedance measurements. *Journal of Applied Electrochemistry*, 29(2):229–238, Feb 1999. ISSN 1572-8838. doi: 10.1023/A:1003481418291. URL https://doi.org/10.1023/A:1003481418291.

[54] F. Mansfeld and M. W. Kendig. Evaluation of anodized aluminum surfaces with electrochemical impedance spectroscopy. *Journal of The Electrochemical Society*, 135(4):828–833, apr 1988. doi: 10.1149/1.2095786. URL https://doi.org/10.1149/1.2095786.

[55] Jörg Kärger and Douglas M. Ruthven. Diffusion in nanoporous materials: fundamental principles, insights and challenges. *New J. Chem.*, 40:4027–4048, 2016. doi: 10.1039/C5NJ02836A. URL http://dx.doi.org/10.1039/C5NJ02836A.

[56] G.E. Thompson and G.C. Wood. Chapter 5 - anodic films on aluminium. In J.C. Scully, editor, *Corrosion: Aqueous Processes and Passive Films*, volume 23 of *Treatise on Materials Science and Technology*, pages 205–329. Elsevier, 1983. doi: https://doi.org/10.1016/B978-0-12-633670-2.50010-3. URL https://www.sciencedirect.com/science/article/pii/B9780126336702500103.

[57] J. A. Davies, B. Domeij, J. P. S. Pringle, and F. Brown. The migration of metal and oxygen during anodic film formation. *Journal of The Electrochemical Society*, 112(7):675, 1965. doi: 10.1149/1.2423662. URL https://doi.org/10.1149/1.2423662.

[58] J. A. Davies, J. P. S. Pringle, R. L. Graham, and F. Brown. A radiotracer study of anodic oxidation. *Journal of The Electrochemical Society*, 109(10):999, 1962. doi: 10.1149/1.2425225. URL https://doi.org/10.1149/1.2425225.

[59] K. Shimizu, G.E. Thompson, G.C. Wood, and Y. Xu. Direct observations of ion-implanted xenon marker layers in anodic barrier films on aluminium. *Thin Solid Films*, 88(3):255–262, 1982. ISSN 0040-6090. doi: https://doi.org/10.1016/0040-6090(82)90054-2. URL https://www.sciencedirect.com/science/article/pii/0040609082900542.

[60] Jude Mary Runge. The metallurgy of anodizing aluminum. *Springer International Publishing*, 2018.

[61] Chuan Cheng and A.H.W. Ngan. Modelling and simulation of self-ordering in anodic porous alumina. *Electrochimica Acta*, 56(27):9998–10008, 2011. ISSN 0013-4686. doi: https://doi.org/10.1016/j.electacta.2011.08.090. URL https://www.sciencedirect.com/science/article/pii/S0013468611013375.

[62] Chuan Cheng and A. H. W. Ngan. Growth sustainability of nanopore channels in anodic aluminum oxide guided with prepatterns. *The Journal of Physical Chemistry C*, 117(23):12183–12190, Jun 2013. ISSN 1932-7447. doi: 10.1021/jp4028436. URL https://doi.org/10.1021/jp4028436.

[63] H. Takahashi and M. Nagayama. The determination of the porosity of anodic oxide films on aluminium by the pore-filling method. *Corrosion Science*, 18(10):911–925, 1978. ISSN 0010-938X. doi: https://doi.org/10.1016/0010-938X(78)90012-4. URL https://www.sciencedirect.com/science/article/pii/0010938X78900124.

[64] Jihun Oh and Carl V. Thompson. The role of electric field in pore formation during aluminum anodization. *Electrochimica Acta*, 56(11):4044–4051, 2011. ISSN 0013-4686. doi: https://doi.org/10.1016/j.electacta.2011.02.002. URL https://www.sciencedirect.com/science/article/pii/S001346861100212X.

[65] A. P. Li, F. Müller, A. Birner, K. Nielsch, and U. Gösele. Hexagonal pore arrays with a 50–420 nm interpore distance formed by self-organization in anodic alumina. *Journal of Applied Physics*, 84(11):6023–6026, 1998. doi: 10.1063/1.368911. URL https://doi.org/10.1063/1.368911.

[66] Matthew R. Jones, Kyle D. Osberg, Robert J. Macfarlane, Mark R. Langille, and Chad A. Mirkin. Templated techniques for the synthesis and assembly of plasmonic nanostructures. *Chemical Reviews*, 111(6):3736–3827, Jun 2011. ISSN 0009-2665. doi: 10.1021/cr1004452. URL https://doi.org/10.1021/cr1004452.

[67] Yiding Liu, James Goebl, and Yadong Yin. Templated synthesis of nanostructured materials. *Chem. Soc. Rev.*, 42:2610–2653, 2013. doi: 10.1039/C2CS35369E. URL http://dx.doi.org/10.1039/C2CS35369E.

[68] Shoso Shingubara. Fabrication of nanomaterials using porous alumina templates. *Journal of Nanoparticle Research*, 5(1):17–30, Apr 2003. ISSN 1572-896X. doi: 10.1023/A:1024479827507. URL https://doi.org/10.1023/A:1024479827507.

[69] Mahmood Tahir, Mazhar Mehmood, Muhammad Nadeem, Abdul Waheed, and Muhammad Tauseef Tanvir. On the variation in the electrical properties and ac conductivity of through-thickness nano-porous anodic alumina with temperature. *Physica B: Condensed Matter*, 425:48–57, 2013. ISSN 0921-4526. doi: https://doi.org/10.1016/j.physb.2013.05.018. URL https://www.sciencedirect.com/science/article/pii/S0921452613003256.

[70] E. Deltombe and M. Pourbaix. The electrochemical behavior of aluminum—potential ph diagram of the system Al-H_2O at 25 c°. *Corrosion*, 14(11):16–20, 11 1958. ISSN 0010-9312. doi: 10.5006/0010-9312-14.11.16. URL https://doi.org/10.5006/0010-9312-14.11.16.

[71] Michael F Ashby and David RH Jones. *Engineering materials 1: an introduction to properties, applications and design*, volume 1. Elsevier, 2012.

[72] T. Shimizu, T. Xie, J. Nishikawa, S. Shingubara, S. Senz, and U. Gösele. Synthesis of vertical high-density epitaxial Si(100) nanowire arrays on a Si(100) sub-

strate using an anodic aluminum oxide template. *Advanced Materials*, 19(7): 917–920, 2007. doi: https://doi.org/10.1002/adma.200700153. URL https://onlinelibrary.wiley.com/doi/abs/10.1002/adma.200700153.

[73] Takashi Yanagishita, Kenji Yasui, Toshiaki Kondo, Yasushi Kawamoto, Kazuyuki Nishio, and Hideki Masuda. Antireflection polymer surface using anodic porous alumina molds with tapered holes. *Chemistry Letters*, 36(4):530–531, 2007. doi: 10.1246/cl.2007.530. URL https://doi.org/10.1246/cl.2007.530.

[74] Mohamed Shaker Salem, Philip Sergelius, Robert Zierold, Josep M. Montero Moreno, Detlef Görlitz, and Kornelius Nielsch. Magnetic characterization of nickel-rich NiFe nanowires grown by pulsed electrodeposition. *J. Mater. Chem.*, 22:8549–8557, 2012. doi: 10.1039/C2JM16339J. URL http://dx.doi.org/10.1039/C2JM16339J.

[75] Leszek Zaraska, Grzegorz D. Sulka, and Marian Jaskuła. Anodic alumina membranes with defined pore diameters and thicknesses obtained by adjusting the anodizing duration and pore opening/widening time. *Journal of Solid State Electrochemistry*, 15(11):2427–2436, Dec 2011. ISSN 1433-0768. doi: 10.1007/s10008-011-1471-z. URL https://doi.org/10.1007/s10008-011-1471-z.

[76] Zenghua He, Lujun Yao, Maojun Zheng, Li Ma, Shuanghu He, and Wenzhong Shen. Enhanced humidity sensitivity of nanoporous alumina films by controlling the concentration and type of impurity in pore wall. *Physica E: Low-dimensional Systems and Nanostructures*, 43(1):366–371, 2010. ISSN 1386-9477. doi: https://doi.org/10.1016/j.physe.2010.08.013. URL https://www.sciencedirect.com/science/article/pii/S1386947710004741.

[77] R.K. Nahar and V.K. Khanna. Ionic doping and inversion of the characteristic of thin film porous Al_2O_3 humidity sensor. *Sensors and Actuators B: Chemical*, 46 (1):35–41, 1998. ISSN 0925-4005. doi: https://doi.org/10.1016/S0925-4005(97)00323-7. URL https://www.sciencedirect.com/science/article/pii/S0925400597003237.

[78] G. E. Thompson and G. C. Wood. Porous anodic film formation on aluminium. *Nature*, 290(5803):230–232, Mar 1981. ISSN 1476-4687. doi: 10.1038/290230a0. URL https://doi.org/10.1038/290230a0.

[79] G. Sauer, G. Brehm, S. Schneider, K. Nielsch, R. B. Wehrspohn, J. Choi, H. Hofmeister, and U. Gösele. Highly ordered monocrystalline silver nanowire arrays. *Journal of Applied Physics*, 91(5):3243–3247, 2002. doi: 10.1063/1.1435830. URL https://doi.org/10.1063/1.1435830.

[80] Kingo Itaya, Shizuo Sugawara, Kunio Arai, and Shozaburo Saito. Properties of porous anodic aluminum oxide films as membranes. *Journal of Chemical Engineering of Japan*, 17(5):514–520, 1984. doi: 10.1252/jcej.17.514.

[81] X. Y. Zhang, L. D. Zhang, Y. Lei, L. X. Zhao, and Y. Q. Mao. Fabrication and characterization of highly ordered Au nanowire arrays. *J. Mater. Chem.*, 11:1732–1734, 2001. doi: 10.1039/B100552I. URL http://dx.doi.org/10.1039/B100552I.

[82] Haibin Tang, Peng Zheng, Guowen Meng, Zhongbo Li, Chuhong Zhu, Fangming Han, Yan Ke, Zhaoming Wang, Fei Zhou, and Nianqiang Wu. Fabrication of hexagonally patterned flower-like silver particle arrays as surface-enhanced raman scattering substrates. *Nanotechnology*, 27(32):325303, jul 2016. doi: 10.1088/0957-4484/27/32/325303. URL https://doi.org/10.1088/0957-4484/27/32/325303.

[83] K. Biswas, Y. Qin, M. DaSilva, R. Reifenberger, and T. Sands. Electrical properties of individual gold nanowires arrayed in a porous anodic alumina template. *physica status solidi (a)*, 204(9):3152–3158, 2007. doi: https://doi.org/10.1002/pssa.200723211. URL https://onlinelibrary.wiley.com/doi/abs/10.1002/pssa.200723211.

[84] Sangwoo Shin, Bo Hyun Kong, Beom Seok Kim, Kyung Min Kim, Hyung Koun Cho, and Hyung Hee Cho. Over 95% of large-scale length uniformity in template-assisted electrodeposited nanowires by subzero-temperature electrodeposition. *Nanoscale Research Letters*, 6(1):467, Jul 2011. ISSN 1556-

276X. doi: 10.1186/1556-276X-6-467. URL https://doi.org/10.1186/1556-276X-6-467.

[85] Jinsub Choi, Guido Sauer, Kornelius Nielsch, Ralf B. Wehrspohn, and Ulrich Gösele. Hexagonally arranged monodisperse silver nanowires with adjustable diameter and high aspect ratio. *Chemistry of Materials*, 15(3):776–779, Feb 2003. ISSN 0897-4756. doi: 10.1021/cm0208758. URL https://doi.org/10.1021/cm0208758.

[86] W.Ch van Geel. On rectifiers. *Physica*, 17(8):761–776, 1951. ISSN 0031-8914. doi: https://doi.org/10.1016/0031-8914(51)90097-3. URL https://www.sciencedirect.com/science/article/pii/0031891451900973.

[87] Nathan J. Gerein and Joel A. Haber. Effect of ac electrodeposition conditions on the growth of high aspect ratio copper nanowires in porous aluminum oxide templates. *The Journal of Physical Chemistry B*, 109(37):17372–17385, Sep 2005. ISSN 1520-6106. doi: 10.1021/jp051320d. URL https://doi.org/10.1021/jp051320d.

[88] A. N. Belov, S. A. Gavrilov, V. I. Shevyakov, and E. N. Redichev. Pulsed electrodeposition of metals into porous anodic alumina. *Applied Physics A*, 102(1):219–223, Jan 2011. ISSN 1432-0630. doi: 10.1007/s00339-010-5907-6. URL https://doi.org/10.1007/s00339-010-5907-6.

[89] Anders B. Laursen, Ana Sofia Varela, Fabio Dionigi, Hank Fanchiu, Chandler Miller, Ole L. Trinhammer, Jan Rossmeisl, and Søren Dahl. Electrochemical hydrogen evolution: Sabatier's principle and the volcano plot. *Journal of Chemical Education*, 89(12):1595–1599, Nov 2012. ISSN 0021-9584. doi: 10.1021/ed200818t. URL https://doi.org/10.1021/ed200818t.

[90] Umberto Lucia. Overview on fuel cells. *Renewable and Sustainable Energy Reviews*, 30:164–169, 2014. ISSN 1364-0321. doi: https://doi.org/10.1016/j.rser.2013.09.025. URL https://www.sciencedirect.com/science/article/pii/S1364032113006965.

[91] Furat Dawood, Martin Anda, and G.M. Shafiullah. Hydrogen production for energy: An overview. *International Journal of Hydrogen Energy*, 45(7):

3847–3869, February 2020. ISSN 03603199. doi: 10.1016/j.ijhydene.2019.12.059. URL https://linkinghub.elsevier.com/retrieve/pii/S0360319919345926.

[92] Yasaman Honarpazhouh, Fatemeh Razi Astaraei, Hamid Reza Naderi, and Omid Tavakoli. Electrochemical hydrogen storage in Pd-coated porous silicon/graphene oxide. *International Journal of Hydrogen Energy*, 41(28):12175–12182, 2016. ISSN 0360-3199. doi: https://doi.org/10.1016/j.ijhydene.2016.05.241. URL https://www.sciencedirect.com/science/article/pii/S0360319915318061.

[93] Manmeet Kaur and Kaushik Pal. Review on hydrogen storage materials and methods from an electrochemical viewpoint. *Journal of Energy Storage*, 23:234–249, 2019. ISSN 2352-152X. doi: https://doi.org/10.1016/j.est.2019.03.020. URL https://www.sciencedirect.com/science/article/pii/S2352152X19301392.

[94] Kasinath Ojha, Soumen Saha, Preeti Dagar, and Ashok K. Ganguli. Nanocatalysts for hydrogen evolution reactions. *Phys. Chem. Chem. Phys.*, 20:6777–6799, 2018. doi: 10.1039/C7CP06316D. URL http://dx.doi.org/10.1039/C7CP06316D.

[95] Zhi Wei Seh, Jakob Kibsgaard, Colin F Dickens, IB Chorkendorff, Jens K Nørskov, and Thomas F Jaramillo. Combining theory and experiment in electrocatalysis: Insights into materials design. *Science*, 355(6321):eaad4998, 2017.

[96] Brian D. Adams and Aicheng Chen. The role of palladium in a hydrogen economy. *Materials Today*, 14(6):282–289, 2011. ISSN 1369-7021. doi: https://doi.org/10.1016/S1369-7021(11)70143-2. URL https://www.sciencedirect.com/science/article/pii/S1369702111701432.

[97] Ho Sun Shin, Jin Yu, Jae Yong Song, and Hyun Min Park. Size dependence of lattice deformation induced by growth stress in Sn nanowires. *Applied Physics Letters*, 94(1):011906, January 2009. ISSN 0003-6951, 1077-3118. doi: 10.1063/1.3064167. URL http://aip.scitation.org/doi/10.1063/1.3064167.

[98] Ho Sun Shin, Jin Yu, Jae Yong Song, Hyun Min Park, and Yong-Sung Kim. Origins of size-dependent lattice dilatation in tetragonal Sn nanowires: Surface stress and growth stress. *Applied Physics Letters*, 97(13):131903, September 2010. ISSN 0003-6951, 1077-3118. doi: 10.1063/1.3493179. URL http://aip.scitation.org/doi/10.1063/1.3493179.

[99] Hui Xu, Hongyuan Shang, Cheng Wang, and Yukou Du. Ultrafine pt-based nanowires for advanced catalysis. *Advanced Functional Materials*, 30(28): 2000793, 2020. doi: https://doi.org/10.1002/adfm.202000793. URL https://onlinelibrary.wiley.com/doi/abs/10.1002/adfm.202000793.

[100] María Escudero-Escribano, Paolo Malacrida, Martin H. Hansen, Ulrik G. Vej-Hansen, Amado Velázquez-Palenzuela, Vladimir Tripkovic, Jakob Schiøtz, Jan Rossmeisl, Ifan E. L. Stephens, and Ib Chorkendorff. Tuning the activity of pt alloy electrocatalysts by means of the lanthanide contraction. *Science*, 352(6281): 73–76, 2016. doi: 10.1126/science.aad8892. URL https://www.science.org/doi/abs/10.1126/science.aad8892.

[101] Mufan Li, Zipeng Zhao, Tao Cheng, Alessandro Fortunelli, Chih-Yen Chen, Rong Yu, Qinghua Zhang, Lin Gu, Boris V. Merinov, Zhaoyang Lin, Enbo Zhu, Ted Yu, Qingying Jia, Jinghua Guo, Liang Zhang, William A. Goddard, Yu Huang, and Xiangfeng Duan. Ultrafine jagged platinum nanowires enable ultrahigh mass activity for the oxygen reduction reaction. *Science*, 354(6318): 1414–1419, 2016. doi: 10.1126/science.aaf9050. URL https://www.science.org/doi/abs/10.1126/science.aaf9050.

[102] Lingzheng Bu, Nan Zhang, Shaojun Guo, Xu Zhang, Jing Li, Jianlin Yao, Tao Wu, Gang Lu, Jing-Yuan Ma, Dong Su, and Xiaoqing Huang. Biaxially strained ptpb/pt core/shell nanoplate boosts oxygen reduction catalysis. *Science*, 354(6318):1410–1414, 2016. doi: 10.1126/science.aah6133. URL https://www.science.org/doi/abs/10.1126/science.aah6133.

[103] Xuesi Wang, Yihan Zhu, Anthony Vasileff, Yan Jiao, Shuangming Chen, Li Song, Bin Zheng, Yao Zheng, and Shi-Zhang Qiao. Strain effect in bimetallic electrocatalysts in the hydrogen evolution reaction. *ACS Energy Letters*, 3

(5):1198–1204, May 2018. doi: 10.1021/acsenergylett.8b00454. URL https://doi.org/10.1021/acsenergylett.8b00454.

[104] Ryan P. Jansonius, Lacey M. Reid, Carolyn N. Virca, and Curtis P. Berlinguette. Strain engineering electrocatalysts for selective co2 reduction. *ACS Energy Letters*, 4(4):980–986, Apr 2019. doi: 10.1021/acsenergylett.9b00191. URL https://doi.org/10.1021/acsenergylett.9b00191.

[105] Chao Zhang, Wei Zhang, Ferdi Karadas, Jingxiang Low, Ran Long, Changhao Liang, Jin Wang, Zhengquan Li, and Yujie Xiong. Laser-ablation assisted strain engineering of gold nanoparticles for selective electrochemical co2 reduction. *Nanoscale*, 14:7702–7710, 2022. doi: 10.1039/D2NR01400A. URL http://dx.doi.org/10.1039/D2NR01400A.

[106] William D. Nix. Mechanical properties of thin films. *Metallurgical Transactions A*, 20(11):2217, Nov 1989. ISSN 1543-1940. doi: 10.1007/BF02666659. URL https://doi.org/10.1007/BF02666659.

[107] X F Yu, X Liu, K Zhang, and Z Q Hu. The lattice contraction of nanometre-sized Sn and Bi particles produced by an electrohydrodynamic technique. *Journal of Physics: Condensed Matter*, 11(4):937–944, jan 1999. doi: 10.1088/0953-8984/11/4/001. URL https://doi.org/10.1088/0953-8984/11/4/001.

[108] Jian Li, Mrityunjay Kothari, S. Chockalingam, Thomas Henzel, Qiuting Zhang, Xuanhe Li, Jing Yan, and Tal Cohen. Nonlinear inclusion theory with application to the growth and morphogenesis of a confined body. *Journal of the Mechanics and Physics of Solids*, 159:104709, February 2022. ISSN 00225096. doi: 10.1016/j.jmps.2021.104709. URL https://linkinghub.elsevier.com/retrieve/pii/S0022509621003239.

[109] W. J. Huang, R. Sun, J. Tao, L. D. Menard, R. G. Nuzzo, and J. M. Zuo. Coordination-dependent surface atomic contraction in nanocrystals revealed by coherent diffraction. *Nature Materials*, 7(4):308–313, April 2008. ISSN 1476-1122, 1476-4660. doi: 10.1038/nmat2132. URL http://www.nature.com/articles/nmat2132.

[110] X. J. Liu, Z. F. Zhou, L. W. Yang, J. W. Li, G. F. Xie, S. Y. Fu, and C. Q. Sun. Correlation and size dependence of the lattice strain, binding energy, elastic modulus, and thermal stability for Au and Ag nanostructures. *Journal of Applied Physics*, 109(7):074319, April 2011. ISSN 0021-8979, 1089-7550. doi: 10.1063/1.3569743. URL http://aip.scitation.org/doi/10.1063/1.3569743.

[111] Q. Jiang, L. H. Liang, and D. S. Zhao. Lattice Contraction and Surface Stress of fcc Nanocrystals. *The Journal of Physical Chemistry B*, 105(27):6275–6277, July 2001. ISSN 1520-6106, 1520-5207. doi: 10.1021/jp010995n. URL https://pubs.acs.org/doi/10.1021/jp010995n.

[112] Jia-Yu Zhang, Xiao-Yong Wang, Min Xiao, L. Qu, and X. Peng. Lattice contraction in free-standing CdSe nanocrystals. *Applied Physics Letters*, 81(11):2076–2078, September 2002. ISSN 0003-6951, 1077-3118. doi: 10.1063/1.1507613. URL http://aip.scitation.org/doi/10.1063/1.1507613.

[113] Chang Q. Sun. Size dependence of nanostructures: Impact of bond order deficiency. *Progress in Solid State Chemistry*, 35(1):1–159, January 2007. ISSN 00796786. doi: 10.1016/j.progsolidstchem.2006.03.001. URL https://linkinghub.elsevier.com/retrieve/pii/S0079678606000173.

[114] Jiankuai Diao, Ken Gall, and Martin L. Dunn. Atomistic simulation of the structure and elastic properties of gold nanowires. *Journal of the Mechanics and Physics of Solids*, 52(9):1935–1962, 2004. ISSN 0022-5096. doi: https://doi.org/10.1016/j.jmps.2004.03.009. URL https://www.sciencedirect.com/science/article/pii/S0022509604000730.

[115] J H Hubbell and S M Seltzer. Tables of x-ray mass attenuation coefficients and mass energy-absorption coefficients 1 kev to 20 mev for elements z = 1 to 92 and 48 additional substances of dosimetric interest, May 1995. URL https://www.osti.gov/biblio/76335.

[116] Bertram Eugene Warren. *X-ray Diffraction*. Courier Corporation, 1990.

[117] Charles Kittel. *Introduction to Solid state Physic*. John Wiley & Sons, eighth edition, 2004.

[118] Des McMorrow and Jens Als-Nielsen. *Elements of modern X-ray physics*. John Wiley & Sons, 2011.

[119] R. E. Dinnebier and S. J. L. Billinge, editors. *Powder Diffraction*. The Royal Society of Chemistry, 2008. ISBN 978-0-85404-231-9. doi: 10.1039/9781847558237. URL http://dx.doi.org/10.1039/9781847558237.

[120] Lachlan M. D. Cranswick. *An Overview of Powder Diffraction*. John Wiley & Sons, Ltd, 2009. ISBN 9781444305487. doi: https://doi.org/10.1002/9781444305487.ch1. URL https://onlinelibrary.wiley.com/doi/abs/10.1002/9781444305487.ch1.

[121] Dominik Kriegner, Zdeněk Matěj, Radomír Kužel, and Václav Holý. Powder diffraction in Bragg–Brentano geometry with straight linear detectors. *Journal of Applied Crystallography*, 48(2):613–618, Apr 2015. doi: 10.1107/S1600576715003465. URL https://doi.org/10.1107/S1600576715003465.

[122] Fabia Gozzo, A. Cervellino, Matteo Leoni, Paolo Scardi, A. Bergamaschi, and B. Schmitt. Instrumental profile of mythen detector in debye-scherrer geometry. *Z. Kristallogr.*, 225(12):616–624, 2010. doi: doi:10.1524/zkri.2010.1345. URL https://doi.org/10.1524/zkri.2010.1345.

[123] Helmut Dosch. *Critical phenomena at surfaces and interfaces: evanescent X-ray and neutron scattering*, volume 126. Springer, 2006.

[124] P. Scherrer. *Bestimmung der inneren Struktur und der Größe von Kolloidteilchen mittels Röntgenstrahlen*, pages 387–409. Springer Berlin Heidelberg, Berlin, Heidelberg, 1912. ISBN 978-3-662-33915-2. doi: 10.1007/978-3-662-33915-2_7. URL https://doi.org/10.1007/978-3-662-33915-2_7.

[125] Yendrapati Taraka Prabhu, Kalagadda Venkateswara Rao, Vemula Sesha Sai Kumar, and Bandla Siva Kumari. X-ray analysis by williamson-hall and size-strain plot methods of zno nanoparticles with fuel variation. *World Journal of Nano Science and Engineering*, 2014, 2014.

[126] H. M. Rietveld. A profile refinement method for nuclear and magnetic structures. *Journal of Applied Crystallography*, 2(2):65–71, Jun 1969. doi: 10.1107/S0021889869006558. URL https://doi.org/10.1107/S0021889869006558.

[127] M. Sakata and M. J. Cooper. An analysis of the Rietveld refinement method. *Journal of Applied Crystallography*, 12(6):554–563, Dec 1979. doi: 10.1107/S002188987901325X. URL https://doi.org/10.1107/S002188987901325X.

[128] P. Thompson, D. E. Cox, and J. B. Hastings. Rietveld refinement of Debye–Scherrer synchrotron X-ray data from Al_2O_3. *Journal of Applied Crystallography*, 20(2):79–83, Apr 1987. doi: 10.1107/S0021889887087090. URL https://doi.org/10.1107/S0021889887087090.

[129] Hugo M Rietveld. The Rietveld method. *Physica Scripta*, 89(9):098002, aug 2014. doi: 10.1088/0031-8949/89/9/098002. URL https://dx.doi.org/10.1088/0031-8949/89/9/098002.

[130] L. B. McCusker, R. B. Von Dreele, D. E. Cox, D. Louër, and P. Scardi. Rietveld refinement guidelines. *Journal of Applied Crystallography*, 32(1):36–50, Feb 1999. doi: 10.1107/S0021889898009856. URL https://doi.org/10.1107/S0021889898009856.

[131] Brian H. Toby. R factors in Rietveld analysis: How good is good enough? *Powder Diffraction*, 21(1):67–70, 2006. doi: 10.1154/1.2179804.

[132] André Guinier, Gérard Fournet, and Kenneth L Yudowitch. *Small-angle scattering of X-rays*. Wiley New York, 1955.

[133] Brian Richard Pauw. Everything saxs: small-angle scattering pattern collection and correction. *Journal of Physics: Condensed Matter*, 25(38):383201, aug 2013. doi: 10.1088/0953-8984/25/38/383201. URL https://dx.doi.org/10.1088/0953-8984/25/38/383201.

[134] Andrei V. Petukhov, Janne-Mieke Meijer, and Gert Jan Vroege. Particle shape effects in colloidal crystals and colloidal liquid crystals: Small-angle x-ray scat-

tering studies with microradian resolution. *Current Opinion in Colloid & Interface Science*, 20(4):272–281, 2015. ISSN 1359-0294. doi: https://doi.org/10.1016/j.cocis.2015.09.003. URL https://www.sciencedirect.com/science/article/pii/S1359029415000643.

[135] M. Rauscher, T. Salditt, and H. Spohn. Small-angle x-ray scattering under grazing incidence: The cross section in the distorted-wave Born approximation. *Phys. Rev. B*, 52:16855–16863, Dec 1995. doi: 10.1103/PhysRevB.52.16855. URL https://link.aps.org/doi/10.1103/PhysRevB.52.16855.

[136] P. Busch, M. Rauscher, D.-M. Smilgies, D. Posselt, and C. M. Papadakis. Grazing-incidence small-angle X-ray scattering from thin polymer films with lamellar structures – the scattering cross section in the distorted-wave Born approximation. *Journal of Applied Crystallography*, 39(3):433–442, Jun 2006. doi: 10.1107/S0021889806012337. URL https://doi.org/10.1107/S0021889806012337.

[137] Rémi Lazzari. *IsGISAXS*: a program for grazing-incidence small-angle X-ray scattering analysis of supported islands. *Journal of Applied Crystallography*, 35 (4):406–421, Aug 2002. doi: 10.1107/S0021889802006088. URL https://doi.org/10.1107/S0021889802006088.

[138] Gennady Pospelov, Walter Van Herck, Jan Burle, Juan M. Carmona Loaiza, Céline Durniak, Jonathan M. Fisher, Marina Ganeva, Dmitry Yurov, and Joachim Wuttke. *BornAgain*: software for simulating and fitting grazing-incidence small-angle scattering. *Journal of Applied Crystallography*, 53(1):262–276, Feb 2020. doi: 10.1107/S1600576719016789. URL https://doi.org/10.1107/S1600576719016789.

[139] Xinhui Lu, Kevin G. Yager, Danvers Johnston, Charles T. Black, and Benjamin M. Ocko. Grazing-incidence transmission X-ray scattering: surface scattering in the Born approximation. *Journal of Applied Crystallography*, 46(1):165–172, Feb 2013. doi: 10.1107/S0021889812047887. URL https://doi.org/10.1107/S0021889812047887.

[140] David B. Williams and C. Barry Carter. *The Transmission Electron Microscope*. Springer US, Boston, MA, 1996. ISBN 978-1-4757-2519-3. doi: 10.1007/978-1-4757-2519-3_1. URL https://doi.org/10.1007/978-1-4757-2519-3_1.

[141] Weilie Zhou, Robert Apkarian, Zhong Lin Wang, and David Joy. Fundamentals of scanning electron microscopy (SEM). In *Scanning microscopy for nanotechnology*, pages 1–40. Springer, 2006.

[142] Lucille A Giannuzzi et al. *Introduction to focused ion beams: instrumentation, theory, techniques and practice*. Springer Science & Business Media, 2004.

[143] R. Jenkins, R. Manne, R. Robin, and C. Senemaud. Iupac—nomenclature system for x-ray spectroscopy. *X-Ray Spectrometry*, 20 (3):149–155, 1991. doi: https://doi.org/10.1002/xrs.1300200308. URL https://analyticalsciencejournals.onlinelibrary.wiley.com/doi/abs/10.1002/xrs.1300200308.

[144] Jianfeng Zhou, Sara Blomberg, Johan Gustafson, Edvin Lundgren, and Johan Zetterberg. Simultaneous imaging of gas phase over and surface reflectance of a Pd(100) single crystal during CO oxidation. *The Journal of Physical Chemistry C*, 121(42):23511–23519, Oct 2017. ISSN 1932-7447. doi: 10.1021/acs.jpcc.7b08108. URL https://doi.org/10.1021/acs.jpcc.7b08108.

[145] S. Pfaff, J. Zhou, U. Hejral, J. Gustafson, M. Shipilin, S. Albertin, S. Blomberg, O. Gutowski, A. Dippel, E. Lundgren, and J. Zetterberg. Combining high-energy x-ray diffraction with surface optical reflectance and planar laser induced fluorescence for operando catalyst surface characterization. *Review of Scientific Instruments*, 90(3):033703, 2019. doi: 10.1063/1.5086925. URL https://doi.org/10.1063/1.5086925.

[146] Lisa Rämisch, Sabrina M. Gericke, Sebastian Pfaff, Edvin Lundgren, and Johan Zetterberg. Infrared surface spectroscopy and surface optical reflectance for operando catalyst surface characterization. *Applied Surface Science*, 578: 152048, 2022. ISSN 0169-4332. doi: https://doi.org/10.1016/j.apsusc.2021.

152048. URL https://www.sciencedirect.com/science/article/pii/S016943322103083X.

[147] Bahaa E.A. Saleh and Malvin Carl Teich. *Fundamentals of photonics*. John Wiley & Sons, 2019.

[148] J. C. Maxwell Garnett and Joseph Larmor. XII. Colours in metal glasses and in metallic films. *Philosophical Transactions of the Royal Society of London. Series A, Containing Papers of a Mathematical or Physical Character*, 203 (359-371):385–420, 1904. doi: 10.1098/rsta.1904.0024. URL https://royalsocietypublishing.org/doi/abs/10.1098/rsta.1904.0024.

[149] Vadim A. Markel. Introduction to the Maxwell Garnett approximation: tutorial. *J. Opt. Soc. Am. A*, 33(7):1244–1256, Jul 2016. doi: 10.1364/JOSAA.33.001244. URL https://opg.optica.org/josaa/abstract.cfm?URI=josaa-33-7-1244.

[150] Colby A. Foss, Gabor L. Hornyak, Jon A. Stockert, and Charles R. Martin. Optical properties of composite membranes containing arrays of nanoscopic gold cylinders. *The Journal of Physical Chemistry*, 96(19):7497–7499, September 1992. ISSN 0022-3654, 1541-5740. doi: 10.1021/j100198a004. URL https://pubs.acs.org/doi/10.1021/j100198a004.

[151] S. N. Paglieri and J. D. Way. Innovations in palladium membrane research. *Separation and Purification Methods*, 31(1):1–169, 2002. doi: 10.1081/SPM-120006115. URL https://doi.org/10.1081/SPM-120006115.

[152] Amit Kumar Chawla, Shikha Wadhwa, Arka Bikash Dey, Florian Bertram, Saif A. Khan, Ratnesh Pandey, Mukul Gupta, Vipin Chawla, Akula Umamaheswara Rao, and D.K. Avasthi. In-situ investigation on hydrogenation-dehydrogenation of Pd–Ag alloy films. *International Journal of Hydrogen Energy*, 47(71):30613–30620, 2022. ISSN 0360-3199. doi: https://doi.org/10.1016/j.ijhydene.2022.07.043. URL https://www.sciencedirect.com/science/article/pii/S0360319922030579.

[153] K. Komander, M.V. Moro, S.A. Droulias, J. Müggenburg, G.K. Pálsson, T. Nyberg, D. Primetzhofer, and M. Wolff. Hydrogen site location in ultrathin vana-

dium layers by N-15 nuclear reaction analysis. *Nuclear Instruments and Methods in Physics Research Section B: Beam Interactions with Materials and Atoms*, 455: 57–60, 2019. ISSN 0168-583X. doi: https://doi.org/10.1016/j.nimb.2019.05.033. URL https://www.sciencedirect.com/science/article/pii/S0168583X19303374.

List of abbreviations

2D-SOR	2-dimensional surface optical reflectance
AAO	Anodic aluminum oxide
AC	Alternating current
BA	Born approximation
BLT	Barrier layer thinning
CV	Cyclic voltammetry
DC	Direct current
DWBA	Distorted-wave Born approximation
EDS	Energy-dispersive x-ray spectroscopy
FIB	Focused ion beam
FWHM	Full-width-half-maximum
GI	Grazing incidence
GIS	Gaseous injection system
GT	Grazing-incidence transmission
HER	Hydrogen evolution reaction
LED	Light-emitting diode
NP-AAO	Nano-porous anodic aluminum oxide
OCP	Open-circuit potential
PAA	Porous anodic alumina
PEEK	Poly ether ether keton
PW	Pore widening
PXRD	Powder x-ray diffraction
SAXS	Small-angle x-ray scattering
SEM	Scanning electron microscopy
SXRD	Surface x-ray diffraction
TEM	Transmission electron microscopy
WAXS	Wide-angle x-ray scattering
XRD	X-ray diffraction
XRF	X-ray fluorescence

Acknowledgements

This PhD has been a once-in-a-lifetime opportunity for me to grow and learn, surrounded by the most brilliant people I have ever met in my life.

First of all, I would like to thank my supervisor Edvin Lundgren. Your door has always been open for questions of any kind, your humour and optimism have been an inspiration. Thank you for your guidance, for giving me your trust and a lot of room to learn. Also, I am very grateful for giving me the opportunity to travel around the world. Before I started I did not even have a passport.

Many thanks to my co-supervisors Gary Harlow, for teaching me electrochemistry and showing me the way from the synchrotron measurement to the publication, and Magnus Borgström for the experiments together and the scientific discussions.

I am very grateful for the substantial contribution of the co-authors of the publications included in this thesis. In particular, I would like to thank Alfred Larsson for his distinguished quality as a colleague, as a scientist and as a friend. Thank you for the tireless scientific discussions and adventures. Also thanks to Andrea Grespi, who holds the record for the highest density of beamtimes in his calendar. Your contribution has been very important. Furthermore, I would like to thank Weronica Linpé for the friendly collaboration to the experiments, Crispin Hetherington, for the meticulous TEM observations; Francesco Carlá and Matthew Snelgrove, for the exceptional experimental support at beamline I07 (Diamond Light Source); Ulrich Lienert, Malte Blankenburg and Zoltan Hegedüs for the great user support at beamline P21.2 (Petra III). A special thanks to Tim Weber, Lorena Glatthaar and Herbert Over, who collaborated to some of the key experiments in this thesis with excellence and involvement.

To the whole division of Synchrotron Radiation Research (even those who have only stayed briefly): I thank each one of you for contributing to make our work environment a great one. In particular, I would like to thank my office mate Hanna, Sandra, Virgi, Lukas, Giulio and everyone else who participated to trips, getaways and music-making: Valeria, Jack, Konstantin, Veronika and Veronica. Your friendship means a lot to me.

Finally, I would like to thank my parents Maria and Vito, my brother Fabio, my in-laws Rosa, Vito and Alessia for their immeasurable long-distance support. Although my career choice has taken me far away from home, you always root for me. *Dulcis in fundo*, my warmest thank you is for my wife Monica, to whom this thesis is dedicated. It would be a lesser thesis without your strength and support in the every-day life. I hope to be at least as bright as you one day.

Printed by Media-Tryck, Lund 2023 NORDIC SWAN ECOLABEL 3041 0903

ISBN 978-91-8039-480-2
Division of Synchrotron Radiation Research
Department of Physics
Faculty of Science
Lund University